DYNAMIC PHENOMENA IN THE LAKES AND SEAS OF TITAN

A Dissertation

Presented to the Faculty of the Graduate School

of Cornell University

in Partial Fulfillment of the Requirements for the Degree of

Doctor of Philosophy

by

Jason Daniel Hofgartner

February 2016

DYNAMIC PHENOMENA IN THE LAKES AND SEAS OF TITAN

Jason Daniel Hofgartner, Ph.D.

Cornell University 2016

Earth and Titan are unique in the Solar System as the only planetary bodies with active hydrologic cycles that include reservoirs of stable, surface liquid. Titan's lakes and seas are primarily composed of methane, ethane, and nitrogen. The buoyancy of frozen solids in these ternary systems is studied. Assuming thermodynamic equilibrium, it is found that frozen solids will float in methane-rich systems for all temperatures below the freezing point. Frozen solids in ethane-rich systems will float if the solid has an air porosity of greater than 10% by volume. For smaller porosities, the buoyancy of the solid in ethane-rich systems changes with temperature and this temperature dependence may result in seasonal oscillations that are unique to Titan. These results have implications for the climatology, geology, and habitability of Titan. Titan's methane hydrologic cycle has been observed to include exchange between the surface and atmospheric reservoirs that is driven by seasonal variation in the distribution of solar energy. Recently, as the summer season approaches in the northern hemisphere, where greater than 99% of Titan's liquids are located, the Cassini orbiter has detected anomalously bright features in the seas. These features are unlikely to be SAR image artifacts or permanent geophysical structures and thus their appearance is the result of an ephemeral phenomenon on Titan. They are found to be more consistent with floating and/or suspended solids, bubbles, and waves than tides, sea level change, and seafloor change and based on the frequency of these phenomena in terrestrial settings, waves is considered to be

the most probable hypothesis. Titan's northern seas are therefore not stagnant liquid bodies but environments where dynamic processes occur. The timing of their appearance suggests that these transients are an expression of the changing seasons.

BIOGRAPHICAL SKETCH

Jason Daniel Hofgartner was born on May 4, 1988 in Windsor, Ontario, Canada to loving parents Martin and Susan Hofgartner. He was blessed to become an older brother to Dieter Hofgartner on September 25, 1989. Jason graduated from Sandwich West Public School in LaSalle, Ontario in 2002 and was the recipient of the Principal's Award for Student Leadership. He graduated from Sandwich Secondary School in LaSalle, Ontario in 2006 and was the recipient of the Principal's Award. Jason earned the Bachelor of Science from the University of Waterloo in 2011 upon completing the honours physics, co-operative program. As an undergraduate student, he was awarded the President's Scholarship of Distinction and the Mike Lazaridis Scholarship in Theoretical Physics. He was employed as a physics research assistant during two co-operative work terms, one at SNOLAB and one at the Perimeter Institute. In his final year as an undergraduate student, he completed research projects under the supervision of Professor Michel Gingras on Spin Ice Physics in Confined Geometrics and the Ewald Technique in Confined Geometrics. Jason earned the Master of Science in astronomy from Cornell University in 2014. As a graduate student, he was awarded the Natural Sciences and Engineering Research Council of Canada Master's and Doctoral Post Graduate Scholarships. Jason was blessed to become a brother-in-law on January 18, 2014 when Dieter married Deborah Hofgartner (Coon). Jason married his best friend Lindsay Maria Hofgartner (Roth) on August 30, 2014 and is blessed to be a son-in-law to loving parents Randy and Ann and brother-in-law to Amy and Garret. During his graduate studies, Jason had the privilege to be advised by Professor Jonathan Lunine and to be co-advised by Professor Alexander Hayes. He was also fortunate to interact with the Cassini-Huygens mission and became an Associate Radar Team Member in 2015. After defending his doctoral dissertation, Jason plans to join NASA's New Horizons mission as a NASA Postdoctoral Program fellow at the Jet Propulsion Laboratory.

I dedicate this dissertation to all who work hard and go out of their way to do the best job they can, even when they are unlikely to be rewarded; their efforts truly make the world a wonderful place.

ACKNOWLEDGEMENTS

I am extremely grateful to my graduate school mentors, Professors Jonathan Lunine and Alexander Hayes. I arrived at Cornell with a dream of preparing for a career that would one day allow me to contribute to the exploration and scientific understanding of other worlds. Professors Lunine and Hayes not only prepared me for such a career, they enabled me to contribute to planetary exploration and science while I was in graduate school and I am immensely appreciative of the opportunities they provided. Among numerous other reasons, I am also especially thankful to Professor Lunine for advising me and nurturing my passion for exploration and science, for always keeping my best interests at the forefront while doing so, and for being an exemplary role model, inside and outside of academia. I am also thankful to Professor Hayes for many more reasons but probably most of all, for regularly involving me in his impressively many endeavors and for his guidance and encouragement throughout the wonderful resultant experiences. They have allowed me to significantly increase my engagement in planetary exploration and science and have been instrumental in my development.

I am also thankful to the Cassini Radar Team for its incredible generosity in permitting me to lead the analysis of very interesting, anomalous features in one of Titan's hydrocarbon seas. Those features were observed because of more than two decades of hard work by the Cassini team and though I had never made any contribution toward the discovery observation, I was allowed to be the leader of their analysis. I can never repay their gift but I aspire to pay it forward in abundance. I also thank the team for its contributions to the analysis of those enigmatic features. I am sincerely thankful to everybody that made the Cassini-Huygens mission and its resultant science a reality.

I also thank the Cornell University community, especially my professors, fellow graduate students, and the Space Sciences Building staff for creating a fantastic environment where intellectual curiosity thrives. I thank all those who helped me to get to Cornell in the first place, including my colleagues at the University of Waterloo, without whom I would not have completed many a problem set, my undergraduate professors, and my schoolteachers.

I am ever grateful to all of my family for a myriad of reasons, including the significant role they have played and continue to play in molding me into the person I am, for providing a tremendous source of inspiration, and for their constant love and support.

I gratefully acknowledge the Natural Sciences and Engineering Research Council of Canada, Post Graduate Scholarship Master's and Doctoral programs and the Cassini project for funding.

Most importantly, I thank God for all things.

TABLE OF CONTENTS

LIST OF FIGURES

LIST OF TABLES

CHAPTER 1

INTRODUCTION

The existence of hydrocarbon lakes and seas at the surface of Saturn's largest moon, Titan, has been well established by the Cassini-Huygens mission. The Cassini Titan RADAR Mapper has discovered hundreds of dark features in both the north and south polar regions that are interpreted as liquid-filled basins based on their near-zero radar reflectivities, location in topographic depressions, and morphologic similarities to terrestrial marine environments including associated channels (Stofan et al., 2007; Hayes et al., 2008). Figure 1.1 is a false color mosaic of Cassini RADAR observations of Titan's north polar region and includes the majority of its liquid hydrocarbon bodies. These lakes and seas are also dark in Cassini Imaging Science Subsystem (ISS) and Visual Infrared and Mapping Spectrometer (VIMS) images and liquid ethane has been spectroscopically identified in the south polar lake, Ontario Lacus (Brown et al., 2008). Specular reflections from Ontario Lacus and the north polar lake and sea, Jingpo Lacus and Ligeia Mare, constrain their surfaces to be extremely smooth with slopes of less than 0.05° and vertical deviations of only a few mm, significantly smoother than expected for solid surfaces (Wye et al., 2009; Stephan et al., 2010; Barnes et al., 2011; Zebker et al., 2014). Ligeia Mare, was also discovered to have a reflective interface beneath its surface, interpreted as the seafloor, and the effective radar absorption of the sea was measured to be very small, consistent with liquid hydrocarbons with little to no impurities (Mastrogiuseppe et al., 2014). Thus Titan is unique in the Solar System as the only extraterrestrial world known to presently host stable, surface liquids.

Titan's lakes and seas interact with and cycle between its atmosphere and

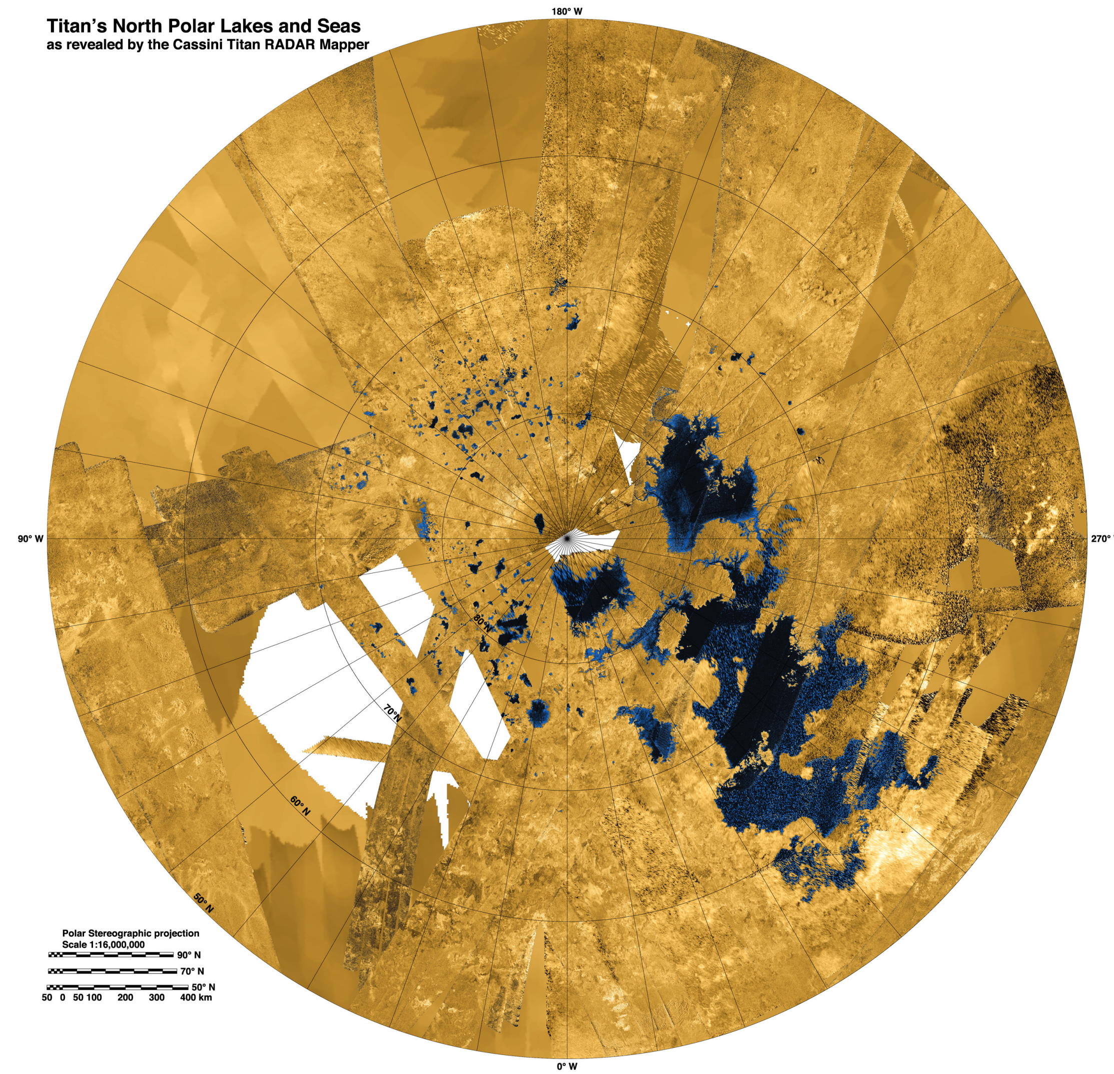

Figure 1.1: Mosaic of Cassini Titan RADAR Mapper observations of Titan's north polar region. The Cassini RADAR observations in this mosaic were obtained in multiple operating modes with resolutions of 0.3-200 km. False coloring is used to distinguish liquid hydrocarbon bodies (black-blue) from solid surfaces (yellow-brown). Kraken Mare is Titan's largest sea and appears to include three basins extending from approximately 45 – 80°N and 280 – 330°W. Ligeia Mare, centered at approximately 80°N, 250°W, is Titan's second largest and most observed sea. Figure 1.2 is a higher zoom image of Ligeia Mare. Punga Mare is the smallest and located most northerly of Titan's three seas. All other surface liquid bodies are smaller than the seas and classified as lakes. Image credit: NASA/JPL-Caltech/ASI/USGS.

solid surface on multiple time scales. Photolysis in Titan's upper atmosphere is gradually depleting its methane via hydrogen escape and the present surface-atmosphere reservoir will be depleted in $10^7 - 10^8$ years. Widespread organic deposits on Titan's surface that are presumed to be methane photolysis products, especially large equatorial dune fields, constitute a larger inventory of hydrocarbons than the surface-atmosphere methane. This suggests that the atmospheric methane has existed for longer than 10^8 years (Lorenz et al., 2008). Outgassing of the interior is a possible source for the methane and could periodically replenish the atmosphere (ex. Tobie et al. (2006)). Atmospheric argon isotope abundance ratios indicate outgassing has occurred (Niemann et al., 2010). On Croll-Milankovitch type orbital-evolution timescales, Titan's hydrocarbon liquids are predicted to oscillate between the north and south polar regions (Lora et al., 2014). The present hemispheric asymmetry in the liquid distribution along with the flooded morphology of seas in the north and dry basins interpreted as sites of paleoseas in the south are regarded as evidence for this oscillation (Aharonson et al., 2009). Over the approximately 30 year seasonal timescale of the Saturn/Titan solar orbit, the changing distribution of solar insolation is predicted to result in hydrologic cycling through evaporation and precipitation. The Cassini spacecraft has gradually observed Titan's seasonal hydrologic cycle during its more than 11 years in the Saturn system. Surface darkening, most likely due to precipitation, the disappearance of small lakes and shoreline recession of Ontario Lacus, most likely due to evaporation and/or infiltration were all observed in the south polar region during the southern summer (Turtle et al., 2011b; Hayes et al., 2011). After the vernal equinox, surface darkening followed by brightening beyond the initial albedo and subsequent reversion back to the initial state, most likely due to precipitation followed by evaporative freezing and subsequent sublimation, was observed over an expansive southern tropical region (Turtle et al., 2011a; Barnes et al., 2013). Numerous additional dynamic phenomena and liquid-atmosphere, liquid-surface interactions such as currents (Tokano et al., 2014; Tokano and Lorenz, 2015), waves (Hayes et al., 2013), and fluvial sediment transport (Burr et al., 2006) are also predicted to occur and to have a seasonal dependence. Observations of these dynamic phenomena as they are occurring however, have thus far been sparse. In late northern winter, the north polar sea, Kraken Mare, exhibited rapid changes in its specular flux that were not consistent with a static model (Barnes et al., 2011) and one of its estuaries exhibited backscatter variations that were unlikely to be from processing artifacts, geometric effects, and varying liquid depth (Hayes et al., 2011). In northern spring, isolated rough patches from waves or mudflats were observed in the northern sea, Punga Mare (Barnes et al., 2014). Theory and observation are employed in this dissertation to further elucidate dynamic phenomena in the lakes and seas of Titan.

In chapter 2 Titan's lakes and seas are modeled as methane-ethane-nitrogen systems and the buoyancy of frozen solids in these ternary systems is studied. Assuming thermodynamic equilibrium, frozen solids will float in methane-rich systems for all temperatures below the freezing point. For ethane-rich systems, frozen solids with an air porosity of greater than 10% by volume will float. For smaller porosities, the buoyancy of ethane-rich frozen solids is temperature dependent.

In chapter 3 the discovery of anomalously bright features in a Cassini RADAR observation of Ligeia Mare is presented. Figure 1.2 shows a Cassini RADAR mosaic of Ligeia Mare and five observations of the region where the anomalously bright features were discovered. Analysis of these anomalous features shows that they are unlikely to be radar image artifacts or permanent geophysical structures and thus are an expression of an ephemeral phenomenon in a hydrocarbon sea on Titan. The features are most consistent with waves, bubbles, and floating/suspended solids. The timing of their appearance, halfway between the vernal equinox and summer solstice, suggests that these features, the first transients detected in the sea, are an expression of the changing seasons.

As a result of the discovery presented in chapter 3, two additional Cassini RADAR observations targeted the region of the transient features, referred to as TFL1 for Transient Features Ligeia 1, and are analyzed in chapter 4. These two observations are shown in the bottom two panels on the left side of figure 1.2. The region of TFL1 was again anomalously bright in the first of the new observations but not the second. Another transient bright feature in Ligeia Mare, TFL2, was also discovered in the first of the two new observations. These observations strongly affirm the conclusion in chapter 3 that TFL1 is neither an image artifact nor a permanent geophysical structure but an expression of an ephemeral phenomenon on Titan. The new observations and all of the previous high-resolution observations of the region of TFL1 are used to better constrain the ephemeral phenomenon that is responsible for its appearance. TFL1 is found to be more consistent with floating and/or suspended solids, bubbles, and waves than tides, sea level change, and seafloor change. Based on the frequency of these phenomena in terrestrial settings, waves is considered to be the most probable hypothesis.

In summary, Titan is unique in the Solar System as the only extraterrestrial world known to host an active hydrologic cycle that includes reservoirs of stable surface liquid. Titan's hydrologic cycle includes a rich variety of dynamic

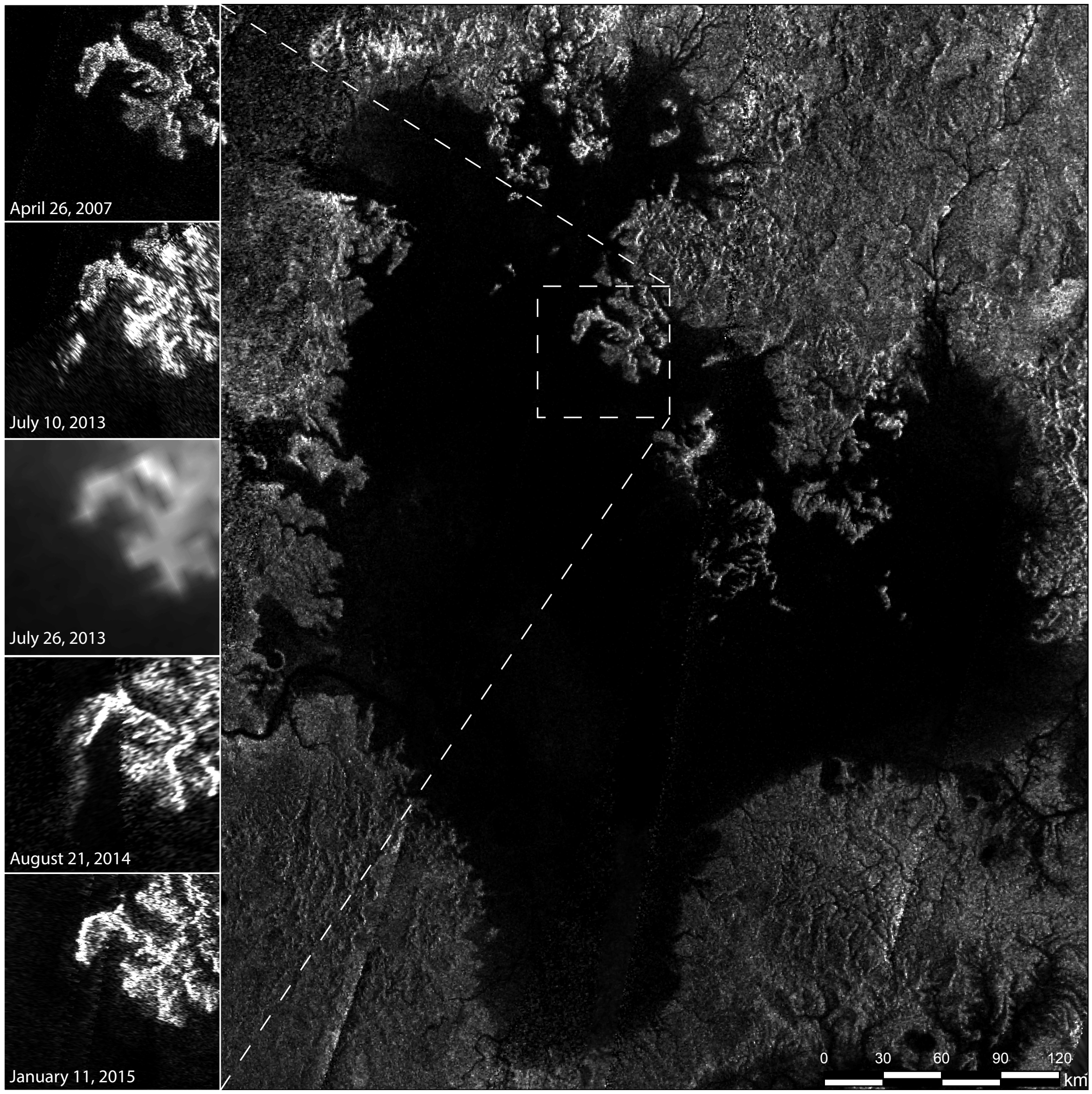

Figure 1.2: Titan's Ligeia Mare and transient bright features. Ligeia Mare is Titan's second largest sea and is located in the north polar region (figure 1.1). Five observations of the region where anomalously bright features were discovered are shown in the panels on the left side of the figure. Anomalously bright features (TFL1) are present in two of the panels (July 10, 2013 and August 21, 2014) but not the other three panels. These transient features are the expression of an ephemeral phenomenon on Titan. The July 10, 2013 observation is overlaid on the April 26, 2007 observation to fill a gap at the top left.

phenomena and marine environments that have created strikingly similar landscapes to those found on Earth. On Titan however, it is methane and ethane, not water that exists as a stable liquid at the surface. This and other differences are expected to enrich the physics of its hydrologic cycle. An example is the possibility for temperature dependence of the buoyancy of frozen solids, which may result in seasonal oscillations that are unique to Titan's lakes and seas. The discovery and confirmation of transient features in one of Titan's hydrocarbon seas by the Cassini spacecraft demonstrates that its seas are not stagnant but rather dynamic environments. Continued study of this hydrologic world should lead to significant insights into planetary hydrologic cycles that will likely have important implications for the understanding of the terrestrial water cycle. Proposals for future exploration of Titan's extraordinary lakes and seas include maritime vessels, aerial vehicles, and orbital spacecraft (Stofan et al., 2013; Lorenz et al., 2015; Barnes et al., 2012; Coustenis et al., 2009; Sotin et al., 2011).

CHAPTER 2

DOES ICE FLOAT IN TITAN'S LAKES AND SEAS?

Originally published in Hofgartner, J. D., Lunine, J. I., Mar. 2013. Does ice float in Titan's lakes and seas? Icarus 223, 628-631.

Abstract

We model Titan's lakes and seas as methane-ethane-nitrogen systems and model the buoyancy of solids in these systems assuming thermodynamic equilibrium. We find that ice will float in methane–rich lakes for all temperatures below the freezing point of pure methane and that ice will also float in ethane–rich seas provided the ice has an air porosity of greater than 5% by volume.

2.1 Introduction

The Cassini RAdio Detection And Ranging (RADAR) instrument has detected standing liquid in both the north and south polar regions of Titan's surface (Stofan et al., 2007; Lunine et al., 2009). The presence of liquid ethane in the south polar Ontario Lacus was confirmed using Cassini's Visual Infrared and Mapping Spectrometer (VIMS) instrument (Brown et al., 2008). Furthermore, the Huygens probe which landed near Titan's equator, is believed to have landed in a dry lake bed, based on geomorphological characteristics of the surrounding surface (Tomasko et al., 2005). The discovery of hydrocarbon lakes and seas makes Titan the only body in the Solar System, aside from the Earth, known to have liquid on its surface. While only liquid ethane has been confirmed on

Titan's surface, the lakes and seas may also be composed of significant amounts of methane and propane (Cordier et al., 2009). Methane and ethane both have triple points near to the temperatures and pressures observed at the surface of Titan and may exist in all three phases at the surface (Cordier et al., 2009); propane's triple point is well below the minimum surface temperature on Titan.

The fact that water ice floats in water is an important aspect of Earth's hydrological cycle and may have been significant to the preservation of life on Earth during times of near-global ice cover. Until now however the fate of solids formed from the freezing of Titan's lakes and seas has not been studied quantitatively, though many qualitative statements are found in the literature that the ice will always sink. The range of parameters that lead to floating ice is of particular interest and may be relevant to the future exploration of Titan (Stofan et al., 2007). Roe and Grundy (2012) recently studied the buoyancy of ice in the methane-nitrogen system and their results provide a good check in the limit of a pure methane-nitrogen lake. From the results of thermodynamic calculations (cf. Cordier et al. (2009)), however, ethane is present or even dominates the composition of lakes and seas that are in equilibrium with Titan's atmosphere; therefore it is important to include ethane in models of these systems. In this note we show that for model lakes and seas composed of methane-ethane-nitrogen mixtures, lakes and seas on Titan can have ice that floats. Ice will float in mixed methane-ethane lakes on the methane–rich side of the binary phase diagram, for all temperatures below the freezing point of pure methane. Ice will also float in ethane–rich lakes provided the ice has an air porosity of greater than 5% by volume.

2.2 Model Lake and Lake Ice

2.2.1 Composition of the Lake and Ice

Ethane-rich seas will contain methane and propane as secondary components (Cordier et al., 2009). However, given the importance of nitrogen in Titan's atmosphere (95% N_2 by mole fraction (Fulchignoni et al., 2005)), it may be present in amounts of several percent up to 20% in the lakes and seas depending on the methane mole fraction (Lunine et al., 1983). Unfortunately, we have not been able to find published experimental data for an ethane-methane-propane-nitrogen system at the temperatures of interest. In fact, the literature appears to contain no data for any ternary combination of the above four compounds at relevant temperatures. Thus to construct our model lake we use thermodynamic data for a methane-ethane binary mixture as well as data about the dissolution of nitrogen in methane and ethane separately. We model the lakes on Titan as methane-ethane-nitrogen mixtures and ignore the small influence of propane in the system.

Surface temperatures in the high latitudes have only modest seasonal swings. Jennings et al. (2009) found from observations of Titan's surface brightness with the Cassini Composite Infrared Spectrometer that in late northern winter the temperature near the northern and southern poles is approximately 91 and 92 K respectively. Cassini radio occultations measure near-surface temperatures near the summer southern pole to be approximately 93 K (Schinder et al., 2012). Schneider et al. (2012), using a general circulation model, predict winter lows near the poles between 90-91 K, and summer highs of 91-92 K. However, the lake energy balance model of Tokano (2009) predicts somewhat larger excursions ranging from just at or below 90 K in winter to 94 K in summer. Our conclusions are the same regarding the propensity of the solid to float whether we take the full range of seasonal temperature swings (90-94K) or a narrower range (91-93 K).

The temperature-composition phase diagram for methane-ethane mixtures at temperatures near the solid-liquid equilibrium, as experimentally determined by Moran (1959)[1], is presented in Figure 2.1. The system is a eutectic system with a minimum freezing point at T = 72.2 K, $X_m = 0.675$. All compositions with a methane mole fraction greater than that at the eutectic point will be referred to as *methane–rich* and all compositions with less methane than the eutectic composition will be referred to as *ethane–rich*. From both the ethane and methane rich sides of the phase diagram, two curves intersect the eutectic point. The higher temperature curves are referred to as the *liquidus curves* and the lower temperature curves as the *solidus curves*. For temperatures and compositions that plot above the liquidus curves and the eutectic point, systems in equilibrium will be in the liquid phase. Methane and ethane liquids are completely miscible in the sense that for all compositions, the system forms a single liquid phase rather than multiple liquid phases of varied composition. For temperatures and compositions that plot below the solidus curves and the eutectic point, systems in equilibrium will be in the solid phase. The miscibility of the solid phases below the eutectic point is not presented in the phase diagram, however Moran (1959) comments that all the systems investigated formed solid solutions, though the deviation from ideal solid solution behavior was considerable. It will be assumed that for temperatures above the eutectic point (i.e. the temperatures pertinent for Titan's surface) the solids are completely mis-

[1]To the extent of the authors knowledge, this is the only experimentally determined phase diagram for methane-ethane systems in this temperature regime.

cible. Finally, in the two remaining regions that are bounded by liquidus and solidus curves, both the liquid and solid phases are stable when the system is at equilibrium.

Consider for example a system that is between the ethane–rich liquidus and solidus curves. For a particular temperature of the system, the compositions of the liquid and solid phases will be given by the intersection of the constant temperature horizontal line with the ethane–rich liquidus and solidus lines respectively. For example, a system at equilibrium with a temperature of 78 Kelvin and a total methane mole fraction of 0.3 ($X_m^t = 0.3$) will have a liquid phase with $X_m^l = 0.455$ and a solid phase with $X_m^s = 0.21$. The relative abundance of the two phases is given by the lever rule (e.g. Rosenberg (1977))

$$\frac{\text{moles of liquid}}{\text{moles of solid}} = \frac{|X_m^s - X_m^t|}{|X_m^l - X_m^t|}. \tag{2.1}$$

For the example system above

$$\frac{\text{moles of liquid}}{\text{moles of solid}} = 0.6. \tag{2.2}$$

To have floating ice (i.e. a situation where both the solid and liquid phases are present when the system is in equilibrium) Titan's lakes must be in one of the two regions of phase space that are between a liquidus and solidus curve.

To include nitrogen in the liquid phase we use the prediction of Lunine and Stevenson (1985) for the solubility of nitrogen in liquid methane-ethane mixtures at the temperatures relevant to Titan's surface. In their work, Lunine and Stevenson assumed that nitrogen obeys Henry's law in the methane and ethane liquids separately and that the Henry's law constant for methane-ethane mixtures behaves ideally. In calculating the molar fraction of nitrogen in the liquid

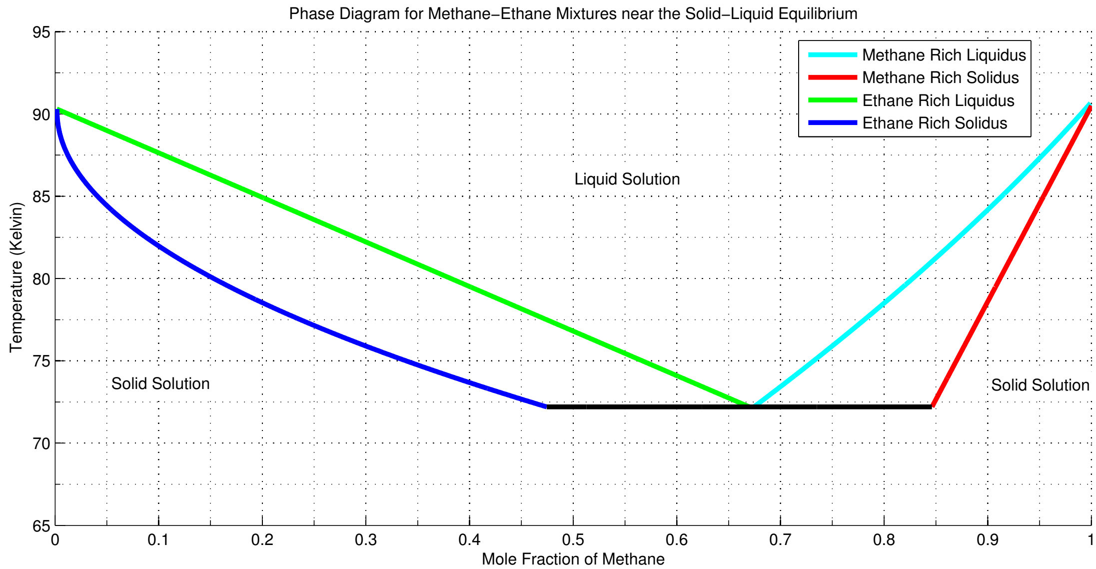

Figure 2.1: Methane-ethane phase diagram. Credit: Moran (1959)

we use their Henry's constant for a total (essentially, nitrogen) pressure at Titan's surface of approximately 1.5 bar (Niemann et al., 2005). Unfortunately, to our knowledge, no similar estimate for the solubility of nitrogen in solid methane-ethane mixtures has been published for the temperatures relevant to Titan's surface. The solubility of nitrogen in pure solid methane has however been determined (Omar et al., 1962) and we use this solubility to estimate the amount of nitrogen dissolved in the methane–rich solids. The solubility of nitrogen in pure solid ethane is unknown and thus we ignore dissolved nitrogen in the ethane–rich solids. This is reasonable since we know from the cases of the liquid mixture and pure solid methane that only a very small (few percent) amount of nitrogen will be dissolved. Furthermore we expect that the difference in chemical structure between N_2 and C_2H_6 will lead to a significant substitution energy necessary to substitute nitrogen for ethane in the crystal structure. Thus the amount of nitrogen dissolved in solid ethane is expected to be less than the amount of nitrogen dissolved in liquid ethane as is the case for methane. Lastly, since we expect any N_2 molecule dissolved in the solid ethane to simply substitute for a C_2H_6 molecule and the atomic masses of these two molecules are very similar (28 amu to 30 amu) we expect the dissolved nitrogen to only minimally affect the density.

2.2.2 Density of the Lake and Ice

To have floating ice it is not only necessary that both the liquid and solid phases are present at equilibrium but also that the liquid phase is denser than the solid phase. Fortunately, in his experiments Moran (1959) also measured the density of the liquid methane-ethane mixtures. For six systems of a particular composition, Moran (1959) measured the density of the liquid phase at various temperatures and fit the density to straight lines of the form

$$\rho^l_{m-e} = E \cdot T + F, \tag{2.3}$$

where ρ^l_{m-e} is the density of the liquid phase, T is the temperature of the system, and E and F are constants. We determined the functional dependence of these constants on composition, yielding a density (in g/mL) of the liquid methane-ethane mixture as a function of both temperature and composition:

$$\rho^l_{m-e} = \frac{-0.1868 \cdot X^l_m - 1.0098}{1000} \cdot T - 0.1766 \cdot X^l_m + 0.7562. \tag{2.4}$$

To determine the density of nitrogen in the liquid phase at these temperatures a curve was fit to the data for the saturation density of liquid nitrogen in the CRC Handbook of Chemistry and Physics (Lide, 2012). The density of the liquid phase is then

$$\rho^l = \frac{\rho^l_{m-e} + \rho^l_n \cdot X_n}{1 + X_n}, \tag{2.5}$$

where the $1 + X_n$ term in the denominator normalizes the liquid to have a total mole fraction of unity.

Moran (1959) did not measure the density of the solid methane-ethane mixtures and no such measurements are published in the scientific literature. Bol'shutkin et al. (1971) however determined the density of pure solid methane for 22 different temperatures, ranging from 11 to 70 Kelvin. Using these data the density of solid methane (in g/mL) as a function of temperature was determined to be

$$\rho_m^s = -5.121 \times 10^{-4} \cdot T + 0.5312. \tag{2.6}$$

Similarly, Klimenko et al. (2008) measured the density of pure solid ethane for 21 different temperatures ranging from 5 to 89.5 Kelvin. From these data the density of solid ethane (in g/mL) as a function of temperature was determined to be

$$\rho_e^s = -88.3301(\frac{T}{1000})^3 + 6.3244(\frac{T}{1000})^2 - 0.2590(\frac{T}{1000}) + 0.7421. \tag{2.7}$$

The density of solid nitrogen in the temperature regime pertinent to Titan's surface is unknown. The density of solid nitrogen at 60 K is known to be $0.949 g/mL$ (Scott, 1976) and we assume this to be the density of solid nitrogen for all temperatures. This is a conservative estimate since we expect the density to decrease with temperature as most substances do and as solid nitrogen does for temperatures below 60K (Scott, 1976). To estimate the density of the solid phase, ideal behavior is assumed such that the density is given by a compositionally weighted sum of the densities of its components. Thus for example the density of ethane–rich solids is

$$\rho^s = X_m \rho_m^s + (1 - X_m)\rho_e^s \tag{2.8}$$

and the density of methane–rich solids is similarly determined with the density of nitrogen as the third component.

2.2.3 Porosity in the Ice

We consider the influence of porosity in the solid phase. Sea ice in oceans on Earth has two types of porosity, brine porosity and air porosity. In our model we only consider the effect of air porosity. The air porosity of sea ice on Earth is quite variable, depending primarily upon the salinity of the ocean water from which it formed and the number of freeze-thaw cycles the ice has experienced but also on a number of other factors. The number of freeze-thaw cycles is important because thawing and refreezing of the ice tends to convert brine porosity to air porosity. Since the influence of brine porosity is not considered in this analysis, the air porosity of first year sea ice that has not experienced a freeze-thaw cycle (and thus not converted its brine porosity to air porosity) is the most relevant. First year sea ice on Earth generally has an air porosity of approximately 0 to 10% by volume (Nakawo, 1983; Kovacs, 1996; Zyryanov, 2012). It is also worth noting that glaciers on Earth which form from an entirely different mechanism than sea ice also tend to have air porosity and the porosity in the Greenland ice cap also varies from approximately 0 to 10% by volume (Schwander et al., 1993). By analogy to water ice on Earth it will be assumed that the porosity of the solid phase in the case of Titan's lakes is somewhere between 0 and 15% by volume.

The porous volume in the ice will be occupied by the air at Titan's surface which is 95% nitrogen and 5% methane. The Huygens probe that landed on Titan's surface in 2005 measured a surface air density of $5.3446 \times 10^{-3} g/mL$ (Fulchignoni et al., 2006). The total density of the solid phase is given by

$$\rho^{\text{solid}} = \frac{V^s\rho^s + V^{\text{porous space}}\rho^{\text{porous space}}}{V^{\text{total}}}, \tag{2.9}$$

but since $V^{\text{total}} = V^s + V^{\text{porous space}}$

$$\rho^{\text{solid}} = (1-\phi)\rho^s + \phi\rho^{\text{porous space}}, \tag{2.10}$$

where ϕ is the fraction of the total volume that is porous.

2.3 Results

The density difference between the equilibrium solid and liquid phases is plotted in Figure 2.2. Both methane and ethane rich systems that have temperatures and compositions that plot between their respective liquidus and solidus curves are included in the figure. For an ethane–rich system at a particular temperature, the equilibrium solid and liquid phases have the composition of the ethane–rich solidus and liquidus curves respectively for that particular temperature. The composition of methane–rich systems is similarly determined. Floating ice corresponds to a negative density difference in the figure. Solids in methane– rich systems are less dense than the coexisting liquid regardless of the air porosity and thus would float. For temperatures near the upper limit investigated (those most relevant to present surface conditions on Titan (Jennings et al., 2009; Schinder et al., 2012), solids in ethane–rich systems require air porosities of greater than approximately 5% in order to float. In the limit of a pure methane-nitrogen system (methane–rich system at 90.7 K), the nitrogen mole fraction in our model lake and ice is approximately 0.23 and 0 respectively and ice will float for this system. This is in agreement with the results of Roe and Grundy (2012) where the ice is pure methane and floats for all liquid nitrogen mole fractions greater than approximately 0.15. We also note that a recent experiment (Luna et al., 2012) found that at 14 Kelvin, the density of solid methane-nitrogen mixtures is less than the density calculated when ideal behavior is assumed (mixture density is given by the compositionally weighted sum of the densities of its components). Thus the density of methane-rich solids may be less than we calculate, which will act to enhance the tendency of the solids to float.

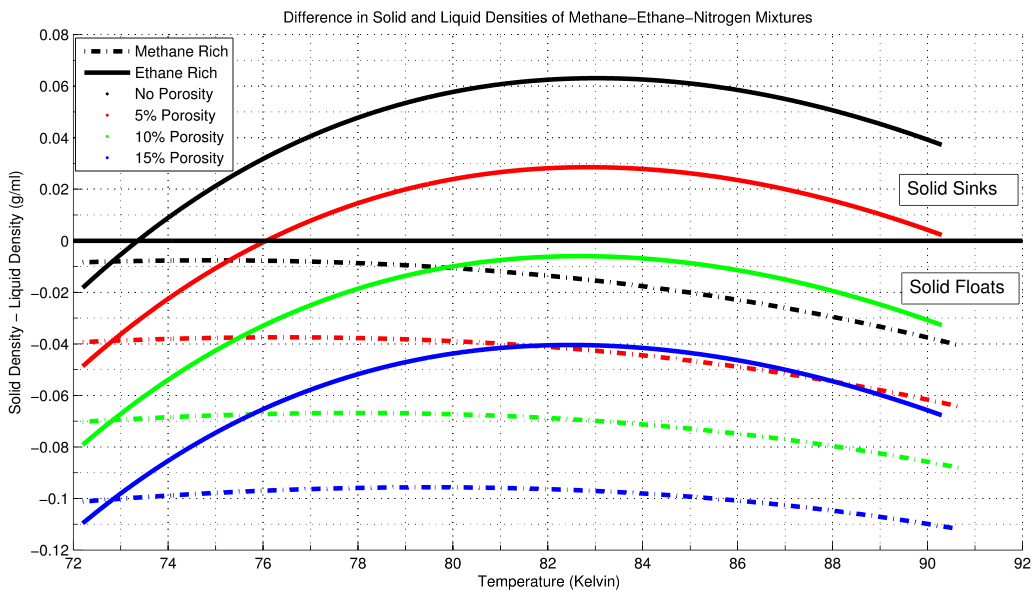

Figure 2.2: Density difference between equilibrium solid and liquid phases in methane-ethane-nitrogen system. Ice will float in Titan's lakes and seas for systems with a negative difference.

2.4 Discussion and Conclusions

For a fairly robust range of parameters, ice formed from the winter freeze-over of Titan's high latitude lakes and seas would float on the coexisting hydrocarbon liquid. Methane–rich lakes will have floating ice for all temperatures below the freezing point of methane (90.7 K) even if the ice does not have any air porosity. The model for methane–rich lakes includes the effect of dissolved nitrogen in both the lake and ice assuming the density behaves ideally. The seas, if ethane–rich, will have floating ice only if the ice forms with a porosity (in which the pores are filled with air that is almost all nitrogen) of greater than approximately 5% by volume, which is plausible based on terrestrial analogs (Nakawo, 1983; Kovacs, 1996; Zyryanov, 2012; Schwander et al., 1993). If upon freezing, Titan's seas are able to incorporate a reasonable air-filled porosity into the ice phase, the ice will float in the lakes. Interestingly, in the case of ethane–rich seas, if the ice forms with an air-filled porosity of between 5 and 10%, the ice will initially float but if the temperature drops by just a few Kelvin the ice will sink. This sensitive dependence of the behavior of the ice on the temperature could lead to some interesting effects. For example, if the surface temperature of the sea oscillates about the point where the solid and liquid have equal density the lake could actually form both ice that floats and sinks. In transitioning from winter to summer a lake could have both ice at its bottom and its surface: Cassini observations of northern hemisphere lakes and seas in the coming few years may see changes in surface reflectivity as spring progresses, in which the liquid surface becomes more and then less reflective as ice rises to the surface and then melts.

Finally, it is possible that some of the differences in radar reflectivities seen by Cassini from lake to lake during the winter (Hayes et al., 2008) might indicate variability in ice cover due in part to variations in the methane mole fraction. Such variation could indicate some of the smaller lakes are not purely rain-fed, but access crustal methane sources. In those cases the formation of floating ice will result in higher reflectivities than lakes with purely liquid surfaces, providing an alternative explanation for the appearance of the so-called "granular" lakes (Hayes et al., 2008). A test of this model will be to observe such lakes as spring progresses in the northern hemisphere; if ice is the cause of the increased reflectivity, the granular lakes should darken in radar images taken now relative to those obtained during the depths of Titan's northern winter.

Acknowledgements

Jason Hofgartner gratefully acknowledges financial support from the Natural Sciences and Engineering Research Council of Canada Post Graduate Scholarship Program and Jonathan Lunine gratefully acknowledges the Cassini Project.

CHAPTER 3

TRANSIENT FEATURES IN A TITAN SEA

Originally published in Hofgartner, J. D., Hayes, A. G., Lunine, J. I., Zebker, H., Stiles, B. W., Sotin, C., Barnes, J. W., Turtle, E. P., Baines, K. H., Brown, R. H., Buratti, B. J., Clark, R. N., Encrenaz, P., Kirk, R. D., Le Gall, A., Lopes, R. M., Lorenz, R. D., Malaska, M. J., Mitchell, K. L., Nicholson, P. D., Paillou, P., Radebaugh, J., Wall, S. D., Wood, C., Jul. 2014. Transient features in a Titan sea. Nature Geoscience 7, 493-496.

Titan's surface-atmosphere system bears remarkable similarities to Earth's, the most striking being an active, global methane cycle akin to Earth's water cycle (Atreya et al., 2006; Lunine and Atreya, 2008). Like Earth's, Titan's seasonal hydrologic cycle is propelled by changes in the distribution of solar energy (Lunine and Atreya, 2008). Indeed, the Cassini Orbiter has witnessed dynamic phenomena at Titan's south pole (Hayes et al., 2011; Turtle et al., 2011b) and equator (Turtle et al., 2011a) following the northward movement of the solar flux. Active processes however, have yet to be confirmed in the northern lakes/seas, which until recently, Cassini never observed in the summer (Lorenz et al., 2010; Hayes et al., 2013; Zebker et al., 2014). But as northern summer solstice approaches, the onset of dynamic phenomena is expected (Lorenz et al., 2010; Hayes et al., 2013; Tokano, 2009, 2013; Roe and Grundy, 2012; Hofgartner and Lunine, 2013). Herein we present the discovery of anomalous, bright features that appeared and disappeared in recent Cassini RADAR data of Titan's northern sea, Ligeia Mare. The most likely explanation for these anomalous features is the occurrence of a transient phenomenon in/on the sea. We find that the ephemeral phenomena most consistent with the observations are surface waves, rising bubbles, and suspended and/or floating solids. This may be only the first observation of many dynamic processes that are commencing in the northern lakes/seas with the change of season.

Anomalous, bright features were detected in Titan's north polar sea, Ligeia Mare, by the Cassini Titan Radar Mapper (RADAR) (Elachi et al., 2004) during the T92 Synthetic Aperture Radar (SAR) pass (Figure 3.1). Three preceding SAR observations (T25, T29, and T64) and a subsequent low-resolution SAR observation (T95) did not detect the anomalous features. The faint, grey spots in the circle of the T95 image are consistent with the speckle noise in the surrounding sea region and thus are not anomalous. Radar backscatter above the noise floor, however, was also detected during preceding T91 radar scatterometry-mode observations (Elachi et al., 2004) but we argue that this signal may not have originated from the anomalies. Subsequent Visual and Infrared Mapping Spectrometer (VIMS) and Imaging Science Subsystem (ISS) observations (T93 and T94) also did not detect the anomalies. These eight passes, constituting all of the high-resolution observations up to the present of the region of the anomalous features, are shown in figure 3.1. In radar images, brightness is determined by the Normalized Radar Cross Section (NRCS), the radar power backscattered to the receiver over the power that would have been received if the power incident on the surface had been scattered isotropically, normalized by the area of the surface (Elachi and van Zyl, 2006). Dynamic processes such as waves (Hayes et al., 2013), suspended particles (Hayes et al., 2011), or bubbles (Engram et al., 2012) increase the NRCS. Such phenomena have not been confirmed in Titan's northern lakes and seas, which have a dielectric constant that indicates a methane-ethane composition and surface height variations of less than 1 mm (Zebker et al., 2014). The progressive seasonal increase in insolation that is occurring however has been predicted to power the onset of energetic processes (Lorenz et al., 2010; Hayes et al., 2013; Tokano, 2009, 2013; Roe and Grundy, 2012; Hofgartner and Lunine, 2013) and we argue that these anomalous features are the observation of transient features in the seas. The regional extent of the anomalous signal, which does not appear to derive from a single contiguous structure but rather from distinct features, is approximately 20 km by 20 km. A higher-zoom image of the anomalous features is provided in appendix A along with further discussion of their morphology. The image formed from the range-Doppler processed, T91 scatterometry-mode signal has noticeably more speckle and lower resolution than the other images because scatterometry-mode observations are not optimized for the formation of range-Doppler processed images (Elachi et al., 2004). We argue that this image still contains credible signal despite the greater speckle.

Hypotheses for the anomalous features detected in the T92 observation, are organized into the following three broad categories. Anomalies could arise from non-geophysical artifacts in the SAR data, permanent, geophysical structures that are only detected when observed with specific geometries, or transitory features that are the result of a surface transformation. We systematically evaluate each of these hypotheses in the following paragraphs.

The appearance of non-geophysical artifacts in SAR images is a familiar problem in radar remote sensing and common artifacts include ambiguities, scalloping, gain control, and edge effects (Elachi and van Zyl, 2006; Stiles et al., 2006). Ambiguities result in a copy or ghost of a region appearing offset in the range and/or azimuth directions. Range ambiguities occur when the radar instrument receives overlapping returns in the time domain from adjacent echo

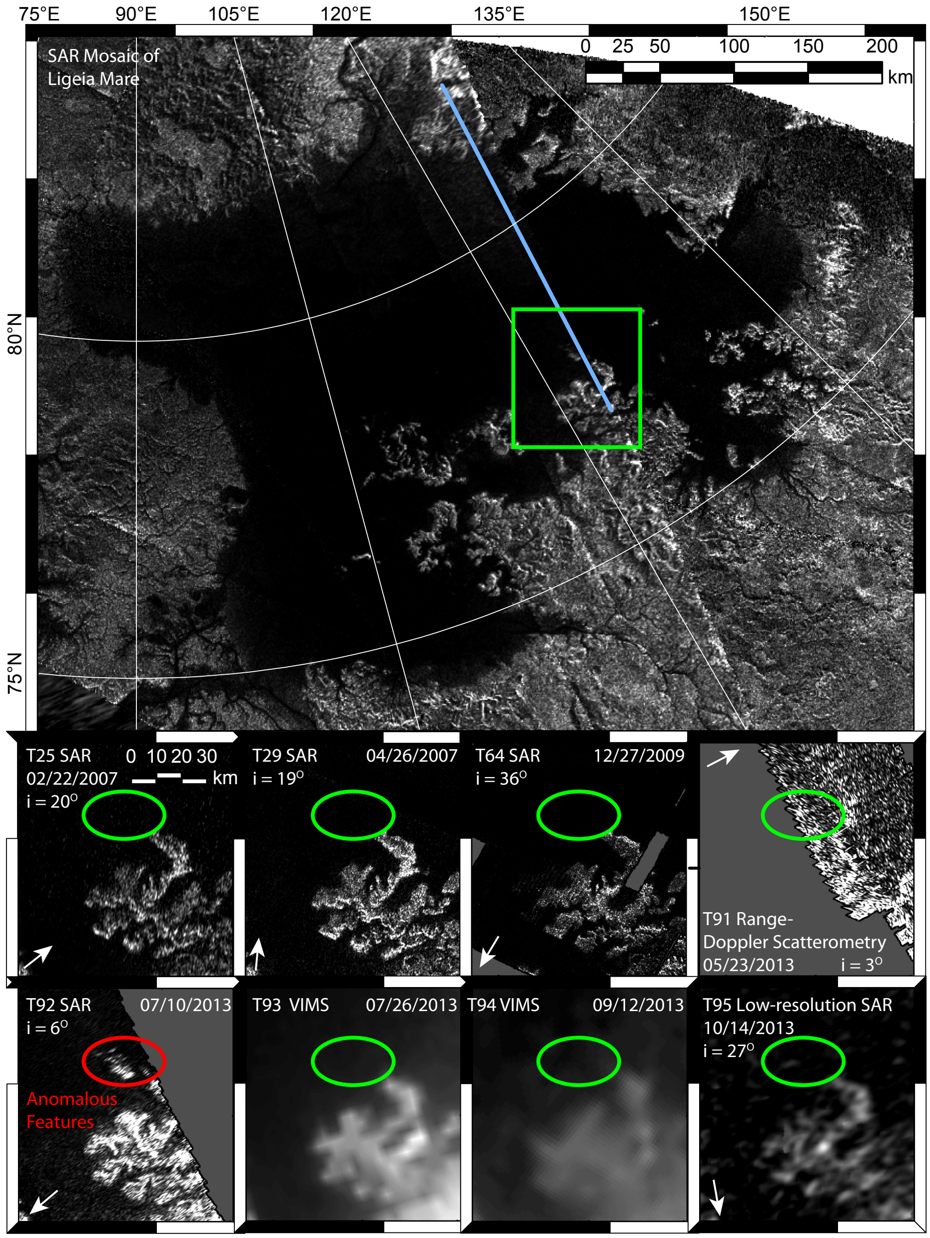

Figure 3.1: Titan's Ligeia Mare and high-resolution Cassini observations of the region of the anomalous features. In the T92 image, anomalous, bright features (circled in red) are observed at 78°N, 123°E that are not seen in any of the other SAR nor VIMS images. Similarly sized, nearby peninsulas (bright region at the bottom right) however were consistently detected. The transient anomalies likely were not present during the T91 scatterometry-mode observation. Pixel brightness is linearly related to NRCS. White arrows in radar images indicate the radar illumination direction. The blue line indicates the transect for figure 3.3.

pulses while azimuth ambiguities arise from aliasing in the frequency domain of an echo. We found that there are no structures that could have resulted in bright range or azimuth ambiguities in the vicinity of the anomalous features. Nadir ambiguities, scalloping, and gain control effects are unlikely to create artifacts that are as spatially confined as the anomalies (Elachi and van Zyl, 2006). The anomalous features are surrounded by dark pixels, indicating that they are unlikely the result of an edge effect. Thus the anomalies are not considered to be standard SAR image artifacts. We provide more detailed arguments in appendix A to support our conclusion that a SAR artifact is not the explanation for the anomalous features.

For Cassini RADAR measurements of a permanent, geophysical structure on Titan, the angle of incidence is the dominant geometrical parameter for the measured NRCS. These two variables are inversely correlated, that is, increasing the angle of incidence decreases the NRCS (Elachi and van Zyl, 2006). Figure 3.2 is a plot of the NRCS from the region of the anomalous features as a function of incidence angle. Only the T91 and T92 observations, at incidence angles of 3 and 6 degrees respectively from the surface normal (black circles), measured radar backscatter above the noise floor (red triangles). Thus any model for the anomalous features as permanent, static structures must be consistent with the T91 and T92 measurements and stay below the noise floor values of the higher incidence angle observations (otherwise the anomalous features would have been detected in those observations as well). Empirically, all terrains on Titan can be well fit by combined quasi-specular and diffuse backscatter models (Wye et al., 2007; Wye, 2011), including the nearby peninsulas (see appendix A), visible toward the lower right in the zoom-panels of figure 3.1. We compared the observations of the anomalies to a suite of quasi-specular plus diffuse backscatter models and found that this class of models for a permanent structure can be ruled out to 88% confidence (see methods section). The best-fit models are plotted in figure 3.2 and their parameters are given in the legend. We also considered models for submerged seamounts, using constraints for the surface roughness and dielectric constant of Ligeia Mare derived from recent analyses of the nadir (0 degrees incidence) signal in the T91 observation (Zebker et al., 2014; Mastrogiuseppe et al., 2014) and found that these models are also ruled out to 88% confidence (see methods section). We note that it is the combination of the small likelihood that the NRCS at 3 degrees is larger than at 6 degrees with the low upper limits at higher incidence angles that inhibits the models from fitting the observations.

We point out that the NRCS upper limits for incidence angles of greater than 15 degrees require that permanent models for the anomalous features not exhibit any appreciable diffuse radar scattering. An absence of diffuse radar scattering however is discordant with the general conclusion, not only from the Cassini spacecraft's 2.2 cm wavelength observations but also from the 3.5 cm and 12.6 cm Earth-based observations, that radar scattering on Titan is dominated by diffuse backscatter (Wye et al., 2007; Wye, 2011; Muhleman et al., 1995; Campbell et al., 2003). The nearby peninsulas for example, exhibit significant diffuse backscatter, as shown by the gray shaded region in figure 3.2. Thus the set of models that has a 12% chance of corresponding to the data has the important caveat that none of those models scatter radar waves diffusely, a behavior that is dissimilar from all other terrains on Titan. Therefore we also consider those models implausible.

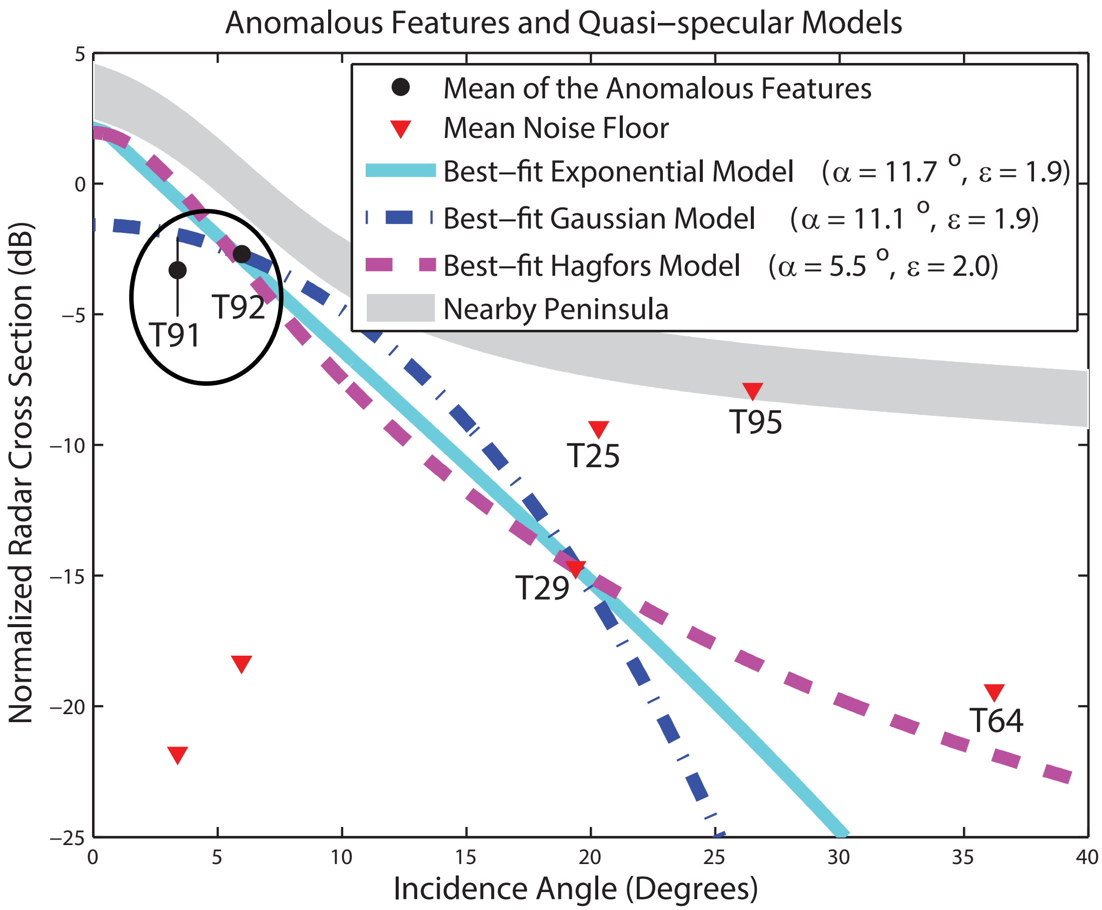

Figure 3.2: Normalized radar cross section of the region of the anomalous features as a function of incidence angle. Only the T91 and T92 observations, at incidence angles of 3.4 and 6.0 degrees respectively (black circles), measured radar backscatter above the noise floor (red triangles). Quasi-specular models are ruled out to 88% confidence because, as shown, the majority cannot simultaneously satisfy the shallow slope between the T91 and T92 observations and the upper limits at higher incidence angles. The grey shaded region shows the behavior of the nearby peninsulas, which is consistent with quasi-specular plus diffuse scattering. Error bars show one-sigma confidence.

The T91 and T92 NRCS profiles along a transect of Titan that crosses Ligeia Mare and includes the region of the anomalous features are plotted in figure 3.3. These profiles, which are both above their respective noise floors, are correlated and the lesser T92 NRCS, relative to that of T91, is due to its greater incidence angle. This behavior is consistent, for example, with the radar transmitting through the liquid and scattering off the seabed as claimed by other analyses (Hayes et al., 2011; Mastrogiuseppe et al., 2014; Hayes et al., 2008, 2010). In the region of the anomalies, however, the T92 profile exhibits a large spike in NRCS while no similar anomalous spike is observed in the T91 profile. Therefore, we conclude that the anomalous features were not present at the time of the T91 observation.

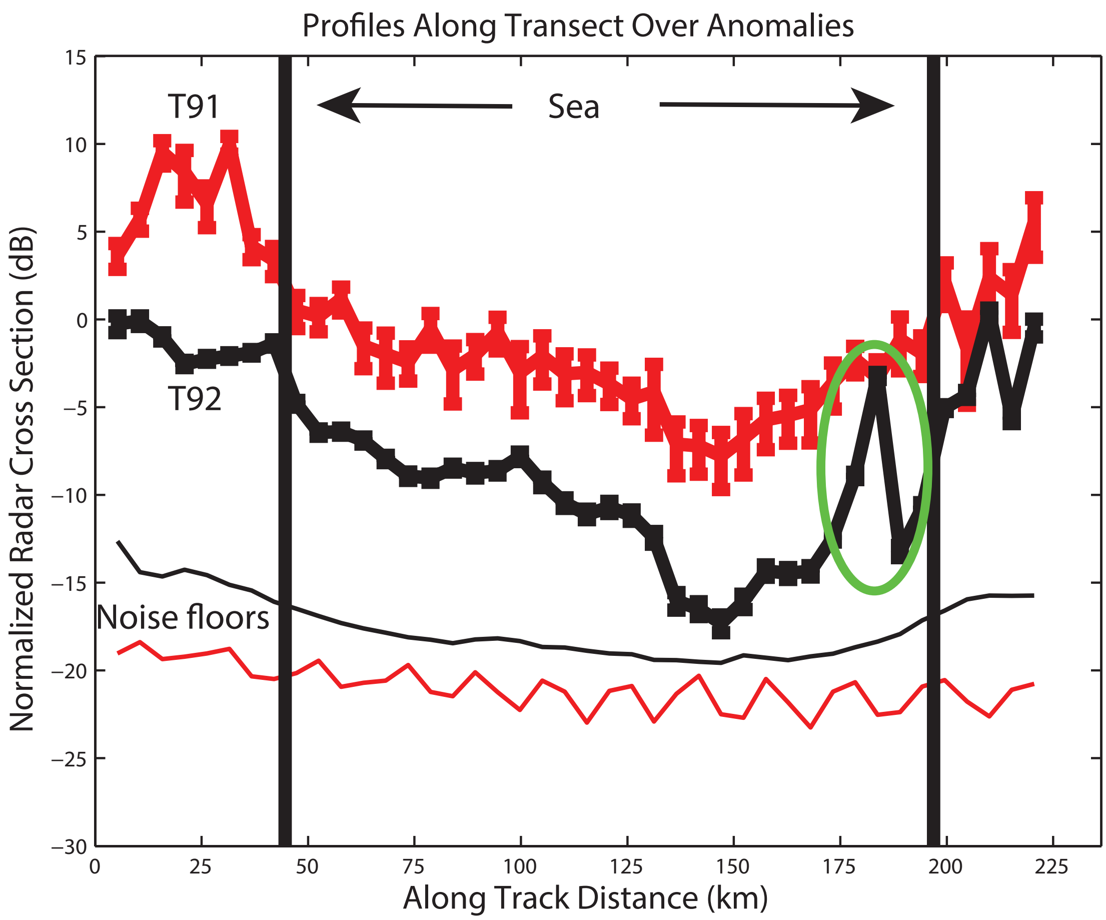

Figure 3.3: Normalized radar cross section profiles along a transect of Titan that crosses Ligeia Mare including the region of the anomalous features. The correlation of the profiles suggests that the signal in the T91 image is valid. At the anomalous features, the T92 profile exhibits a large spike but no similar spike is observed in the T91 profile. Incidence angle increases from $3.3^\circ - 3.5^\circ$ and $4.6^\circ - 6.2^\circ$ for the T91 and T92 observations respectively. The blue line in figure 3.1 indicates the center of the transect. The error bars show the one-sigma confidence.

Transitory hypotheses envisage that a transformation occurred prior to the discovery of the anomalous features and that their detection thus depends primarily on the timing of the observation. The anomalies were not detected in three observations before 2013, were detected in the T92 observation on July 10th, 2013 and then not detected in three subsequent observations (Figure 3.1). A signal was detected in the T91 observation on May 23rd, 2013 but as previously discussed, the transient anomalies likely were not present during this observation. Therefore the evolution of the anomalous features appears to have included a reversion after the T92 pass and we do not consider further hypotheses that predict the formation of a new permanent structure, such as an island via cryovolcanism and restrict further discussion to hypotheses for ephemeral features. From recent analysis of the nadir signal in the T91 observation (Mastrogiuseppe et al., 2014), the absorption of the radar energy as it propagates through the sea is constrained to be small. Thus variations in sea level should not strongly influence the measured NRCS and are unlikely to explain the transient anomalies. With the exception of the T25 and T29 passes, all of the passes occurred at the same true orbital anomaly and thus hypotheses that depend on Titan's orbit around Saturn, such as tides, are also not considered further.

The remaining transient hypotheses include waves, rising bubbles, and suspended and/or floating solids. The data do not permit us to further discard any of these hypotheses with confidence. Titan's northern hemisphere is transitioning from vernal equinox (August 2009) to summer solstice (May 2017) and it is plausible that the anomalous, transient features are an expression of the changing seasons. Waves were/are expected to form and become detectable as wind speeds in the northern hemisphere climb with the approach of summer (Lorenz et al., 2010; Hayes et al., 2013; Tokano, 2009, 2013). Thermal perturbations could lead to the exsolution of gases from the liquid and/or sea floor that form bubbles and buoyantly rise to the surface. Polyacetylene and other low-density solids could be suspended in the sea (Chien, 1984) much like silt in a terrestrial delta, (backscatter variation, possibly from a transient surface layer with distinct dielectric properties, has been previously observed near an estuary of Kraken Mare (Hayes et al., 2011)) and it has been predicted that sunken solids formed from a winter freeze could become buoyant with the onset of warmer temperatures (Hofgartner and Lunine, 2013). This discussion of seasonal mechanisms is not inclusive and all of the remaining hypotheses may have additional plausible mechanisms.

Some of the ephemeral phenomena cited above as causes of the transient radar signature may be stimulated or enhanced by regional meteorological phenomena, such as wind or rain. While Cassini did not detect any clouds during the T92 pass, the geometry was rather unfavorable for detection above the site of the anomalies; we note, however, that during the T93 pass VIMS detected a cloud, approximately 100 km in diameter, about 350 km from the region of the transients.

3.1 Methods

3.1.1 Mask

To determine the mean NRCS of the regions of the anomalous features and thus produce the plot in figure 3.2, it was necessary to define a mask that encompassed exclusively the regions of the anomalous features. We considered a zone that, from visual inspection, included all pixels of the anomalous features as well as some sea pixels but none of the shore. The mask for the anomalies was defined as all pixels in this zone with an NRCS in the T92 image of greater than 0.25 and was used to determine the average characteristics in each observation of the region of the anomalies. The cut-off of 0.25 was selected to eliminate $> 99\%$ of the sea pixels, based on analysis of their backscatter distribution but retain the majority of the pixels of the anomalous features. Since radar measurements of any feature will have an exponential distribution (speckle), a threshold that removes the lower end of the distribution biases the mean NRCS toward a higher value. We found that the cut-off only minimally biased the T92 NRCS and did not significantly affect the results.

3.1.2 Modeling

We considered three classes of quasi-specular models: exponential, Gaussian, and Hagfors (Wye, 2011). To test if the data are consistent with these models, we simulated the T91 and T92 observations by randomly generating NRCS values such that they followed a normal distribution, with the mean and standard deviation given by the observed NRCS and error. We then checked if any models fit the two simulated backscatter measurements and remained below the upper limits at higher incidence angles. The exponential, Gaussian, and Hagfors models failed to fit the data in $> 99\%$, 88%, and $> 99\%$ of the simulations respectively. The best-fit models are plotted in figure 3.2 and their root-mean-square roughnesses and effective dielectric constants are given in the legend. The success rate of Gaussian models was greater than exponential and Hagfors models because they predict a shallower gradient in NRCS at the lowest incidence angles (less than about 10 degrees) and a steeper gradient at higher incidence angles. This is consistent with the measured NRCS, which is approximately flat for the lowest incidence angles but significantly reduced by about 20 degrees incidence.

Including the additional physics of refraction and loss due to reflection at the atmosphere-sea interface (Hayes et al., 2010), we followed the same prescription as above to test models for submerged seamounts. We used the recently measured index of refraction for Ligeia Mare to calculate the refracted incidence angles of the radar (Mastrogiuseppe et al., 2014) and considered a perfectly flat surface for Ligeia Mare, consistent with recent measurements (Zebker et al., 2014), when calculating the Fresnel transmission coefficients.

Acknowledgements

JDH gratefully acknowledges the Cassini RADAR and VIMS Teams for the data and the opportunity to lead the analysis and the Cassini Project and Natural Sciences and Engineering Research Council of Canada, Post Graduate Scholarship Program for financial support. AGH was partially supported by NASA grant NNX13AG03G. A portion of this work was performed at the Jet Propulsion Laboratory, California Institute of Technology under a contract with the National Aeronautics and Space Administration.

Author Contributions

JDH led the analysis and writing of the letter. AGH and JIL worked closely with JDH on all aspects of the analysis and writing. HZ worked closely with JDH on the NRCS analysis. BWS contributed the SAR processing and artifact analysis and that section of the letter. CS, JWB, and EPT contributed to the VIMS and ISS analysis and the cloud discussion. All authors contributed to the data acquisition and discussions.

CHAPTER 4

TITAN'S MAGIC ISLANDS: TRANSIENT FEATURES IN A HYDROCARBON SEA

Originally prepared for submission to Icarus as Hofgartner, J. D., Hayes, A. G., Lunine, J. I., Zebker, H., Lorenz, R. D., Malaska, M. J., Mastrogiuseppe, M., Notarnicola, C., Soderblom, J. M., Titan's Magic Islands: Transient Features in a Hydrocarbon Sea.

Abstract

The region of Titan's hydrocarbon sea, Ligeia Mare, where transient bright features were previously discovered, was anomalously bright in the first of two more recent Cassini RADAR observations but not the second. Another transient bright feature in a different region of Ligeia Mare was also discovered in the first of the new observations. Here we present all the high-resolution observations of the regions containing the transient features and the quantitative constraints that we derived from them. We argue that these features are unlikely to be SAR image artifacts or permanent geophysical structures and thus their appearance is the result of an ephemeral phenomenon on Titan. We find that the transient features are more consistent with floating and/or suspended solids, bubbles, and waves than tides, sea level change, and seafloor change and based on the frequency of these phenomena in terrestrial settings, we consider waves to be the most probable hypothesis. These transient features are the first instance of active processes in Titan's lakes and seas to be confirmed by multiple detections and demonstrate that Titan's seas are not stagnant but rather dynamic environments.

4.1 Introduction

Titan is unique in the Solar System as the only extraterrestrial world known to host an active hydrologic cycle that includes reservoirs of stable, surface liquid (Lunine and Atreya, 2008). The dynamics of Titan's hydrologic cycle and surface liquids have gradually been revealed during the Cassini spacecraft's eleven years in the Saturn system, during which it has acquired data on more than 110 flybys of Titan. In the southern summer season, surface darkening that was most likely due to precipitation (Turtle et al., 2011b) and shoreline recession of lakes due either to evaporation and/or infiltration were observed in the south polar region (Hayes et al., 2011; Turtle et al., 2011b). The albedo of the southern tropical regions, Sotra Patera and Tui Regio, also reportedly increased and decreased respectively at multiple wavelengths in their spectra during the austral summer (Solomonidou et al., in press). In late southern summer, the surfaces of the lakes Ontario Lacus and Jingpo Lacus, near the south and north poles respectively, were constrained to be smooth and likely devoid of surface waves (Wye et al., 2009; Barnes et al., 2011). Kraken Mare, Titan's largest sea and neighbor of Jingpo Lacus, however exhibited rapid changes in flux that were not consistent with a static model, though the exact cause of the changes could not be determined (Barnes et al., 2011). Moray Sinus, an estuary of Kraken Mare, also exhibited radar backscatter variations that could not be explained by processing artifacts or geometric effects and explanations other than varying liquid depth were preferred (Hayes et al., 2011). After vernal equinox, an expansive southern tropical region was darkened by precipitation and then subsequently brightened beyond its initial albedo, possibly due to evaporative freezing, before reverting back to its initial state (Turtle et al., 2011a; Barnes et al., 2013). In northern spring, isolated rough patches attributed to waves or mudflats were observed in the northern sea, Punga Mare (Barnes et al., 2014). Ligeia Mare, Titan's second largest sea and also located in the north polar region, however was constrained to have an extremely flat surface (Zebker et al., 2014). In July 2013, half way between the August 2009 vernal equinox and May 2017 summer solstice, anomalously bright features were discovered in Ligeia Mare (Hofgartner et al., 2014). Hofgartner et al. (2014) argued that these features, all clustered in one region of the sea, are inconsistent with image artifacts and permanent geophysical structures and best explained by the occurrence of ephemeral phenomena such as floating and/or suspended solids, bubbles, and waves.

We present here analysis of two new Cassini RADAR observations of the region of Ligeia Mare where the anomalously bright features were discovered (78°N, 123°E). In the T104 flyby this region of the sea again appeared anomalously bright compared to adjacent regions of the sea. In the T108 flyby, no anomalously bright features were detected in this region or any other observed region of Ligeia Mare. We refer to these features throughout this manuscript as TFL1, short for Transient Features Ligeia 1 and note that they have also been referred to as *Titan's Magic Island* in conferences and the media. When distinguishing between the features in the discovery observation (the Cassini T92 flyby) and the more recent T104 observation, we use the nomenclature TFL1-92 and TFL1-104. This nomenclature is not intended to imply that the two detections correspond to the same transient features observed twice, as opposed to distinct transient features observed at the same location. These two possibilities are discussed later in this manuscript. Rather, we implement this nomenclature so that we can refer to the features in a specific observation. As we will argue below, the T104 and T108 observations strengthen the previous conclusion that

TFL1-92 was not due to image artifacts or permanent geophysical structures but most likely an ephemeral phenomenon on Titan. Thus TFL1 is the first reported transient occurrence in Titan's lakes and seas to be confirmed by subsequent observations. We use these new observations in addition to all previous high-resolution observations of the region of TFL1 to better constrain the ephemeral phenomenon that is responsible for its appearance. We find floating and/or suspended solids, bubbles, and waves to be the most likely hypotheses and based on the frequency of these phenomena in terrestrial settings, we consider waves to be the most probable explanation of TFL1.

We also discovered a second transient feature in Ligeia Mare in the T104 data, centered at 80.5°N, 111.5°E, that was not present in any of the previous observations of this region nor the subsequent T108 observation. We refer to this feature as TFL2 and note that we have previously referred to it as *L2* in conferences. We will argue below that TFL2 is also unlikely to be an image artifact or permanent geophysical structure and thus is an expression of a natural but ephemeral phenomenon on Titan. Floating and/or suspended solids, bubbles, and waves are also the likely hypotheses for TFL2 and we consider waves to be the most probable. Thus both TFL1 and TFL2 are probably expressions of wave fields on Ligeia Mare but the mechanism for generating the waves in each case could have been different.

In the Observations section of this paper we present all the high-resolution observations of the region of TFL1 and the T92 and T104 observations of the region of TFL2. Then we provide the quantitative constraints on TFL1 that were derived from the observations. Appendix B includes all of the high-resolution observations of the region of TFL2 and the quantitative constraints that were derived from them. In the Transient Hypotheses section, the observations and quantitative constraints are used to rule in or out various hypotheses for TFL1. The Discussion section includes consideration of the plausibility of the transient hypotheses and the association of TFL1/TFL2 with Titan's seasons, local meteorology, and their nearby shorelines.

4.2 Observations

4.2.1 TFL1

Figure 4.1 shows a Cassini Synthetic Aperture Radar (SAR) mosaic of Ligeia Mare, Titan's second largest hydrocarbon sea. The region of the transient features in Ligeia Mare, TFL1, has been observed by the Cassini Titan RADAR mapper (Elachi et al., 2004) six times in high resolution SAR mode (T25, T29, T64, T92, T104, and T108), once in low resolution SAR mode (T95), and once in range-Doppler processed off-nadir altimetry mode (T91). The Cassini Visual and Infrared Mapping Spectrometer (VIMS) (Brown et al., 2004) also observed this region twice in high resolution (T93 and T94). These ten observations comprise the set that could have resolved TFL1 were it present and are shown in the lower panels of figure 4.1. Transient bright features are visible in the T92 (TFL1-92) and T104 (TFL1-104) images and are circled in red in the panels with those observations. TFL1-92 is brighter and smaller in area than TFL1-104. While the transient bright signal of TFL1-92 originates from multiple distinct regions (Hofgartner et al., 2014), TFL1-104 appears to originate from a single, contiguous region that is larger in total area. TFL1 is not present in any of the other images. The consistent behavior of the nearby shoreline, toward the bottom right of the panels, argues that the appearance/disappearance of TFL1 is not governed by changes in the characteristics of the observation, such as resolution or geometry but rather is the result of physical changes that are occurring in time.

Together, the T92, T104, and T108 observations in particular, provide strong evidence that TFL1 is unlikely to be explained either by image artifacts or by changes in the characteristics of the observation and is indeed the expression of a transient phenomenon on Titan. Artifacts in a SAR image usually result from aliasing in distance (range) or Doppler frequency (azimuth), hence the location of an artifact will generally vary with viewing geometry. Thus the occurrence of TFL1 at the same location in both the T92 and T104 observations, despite their different illumination directions and incidence angles, indicates that it is not a SAR image artifact. A detailed investigation of TFL1-92 found that it is inconsistent with range and azimuth ambiguities, edge and gain control effects, and scalloping (Hofgartner et al., 2014). The absence of TFL1 in the T108 observation, at an incidence angle intermediate to that of the T92 and T104 observations indicates that it cannot be explained as simply a permanent structure that is only detected at low incidence angle SAR observations. Furthermore, the large difference in the T92 and T104 illumination directions demonstrates that the appearance of the features is also not restricted to a particular azimuth angle. The T25 and T104 observations in fact, differ in their azimuthal angles by just 4 degrees but TFL1 is only present in the latter. Thus TFL1 is most likely the expression of an ephemeral phenomenon. This is in agreement with the analysis of TFL1-92, prior to the T104 and T108 observations, that concluded it was not consistent with a SAR image artifact or a permanent geophysical structure

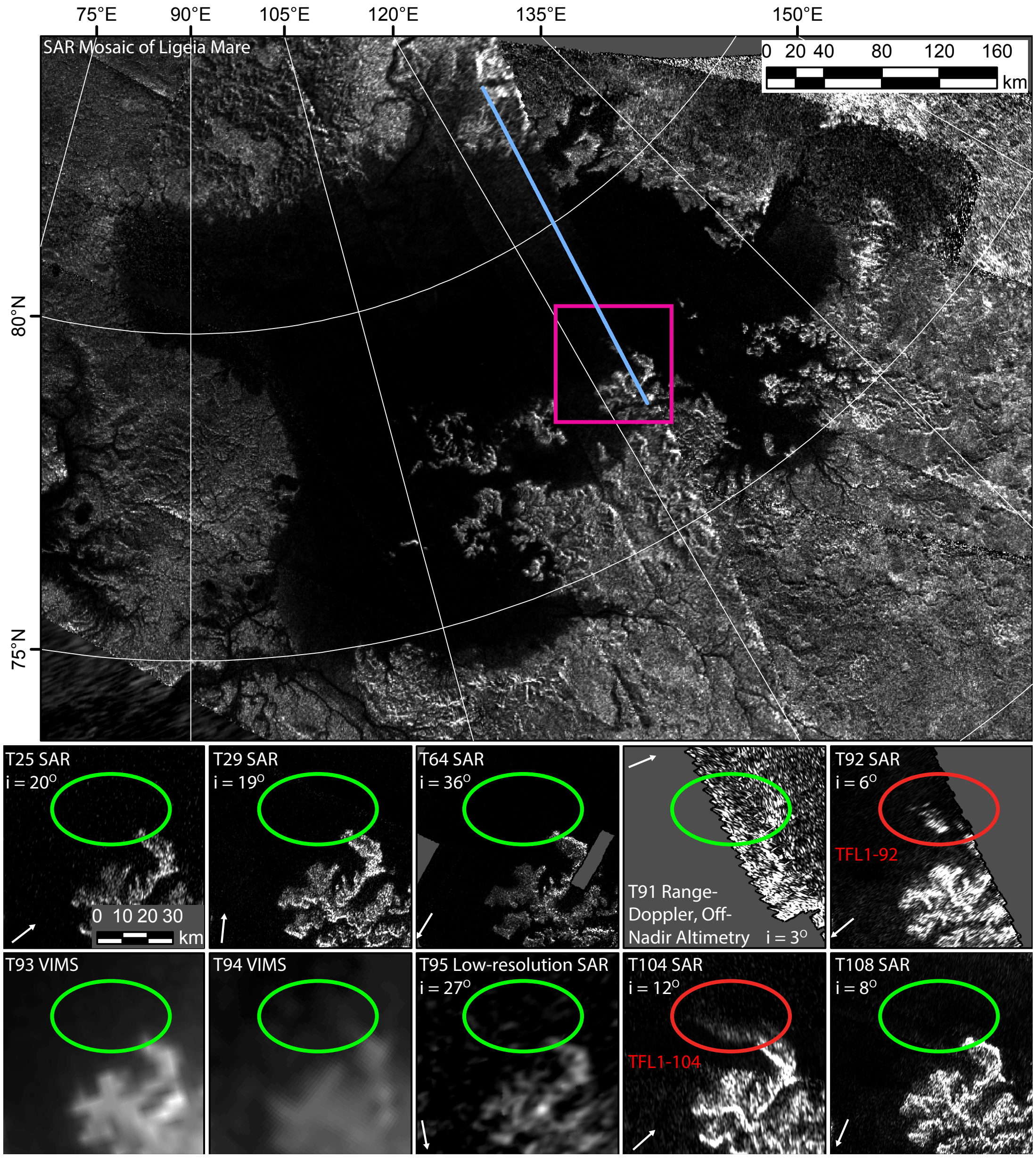

Figure 4.1: Titan's Ligeia Mare and all high-resolution observations of the region of TFL1. Transient bright features, TFL1, are observed in the T92 and T104 observations at 78°N, 123°E (circled in red) that are not seen in any of the other observations. Similarly sized features of the nearby shore toward the lower right however are consistently observed. Pixel brightness is linearly related to the normalized radar cross section in the RADAR images and I/F in the VIMS images. The white arrow in each radar observation indicates the radar azimuthal illumination direction and the subtitle provides the incidence angle. The magenta rectangle indicates the extent of the lower panels and the blue line indicates the length of the transect that is shown in figure 4.4.

(Hofgartner et al., 2014).

We argue below, that TFL1 was not physically present in the T25, T29, T64, T91, and T108 observations. It is unclear however whether TFL1 was present during the T93-T95 observations. Though it was not detected during these observations, it may have been present but not detectable due to the different nature of the passive, near-infrared T93 and T94 VIMS observations and the high noise, high incidence angle combination of the T95 observation. We also note that the brightest parts of TFL1-92 and TFL1-104 are located at approximately the same spatial position. Thus it is possible that the two detections correspond to two different episodes of an ephemeral phenomenon (or even to two unique ephemeral phenomena) but they could also correspond to one continuous episode that included a temporal evolution. We will discuss these possibilities in greater detail.

4.2.2 TFL2

Figure 4.2 shows the T92 and T104 observations of a part of Ligeia Mare that includes the region of TFL2. The region of TFL2, centered at 80.5°N, 111.5°E, has been observed six times in high resolution SAR mode (T25, T29, T64, T92, T104, and T108) and once in range-Doppler processed off-nadir altimetry mode (T91). These seven observations are shown in appendix B. A transient bright feature (TFL2) is present in only the T104 image and is circled in red in figure 4.2. The top of the right panel shows the region of TFL2 (yellow) within the boundary of Ligeia Mare (purple). Like TFL1-104 but unlike TFL1-92, TFL2 appears to originate from a single, contiguous region with an area of 322 km^2.

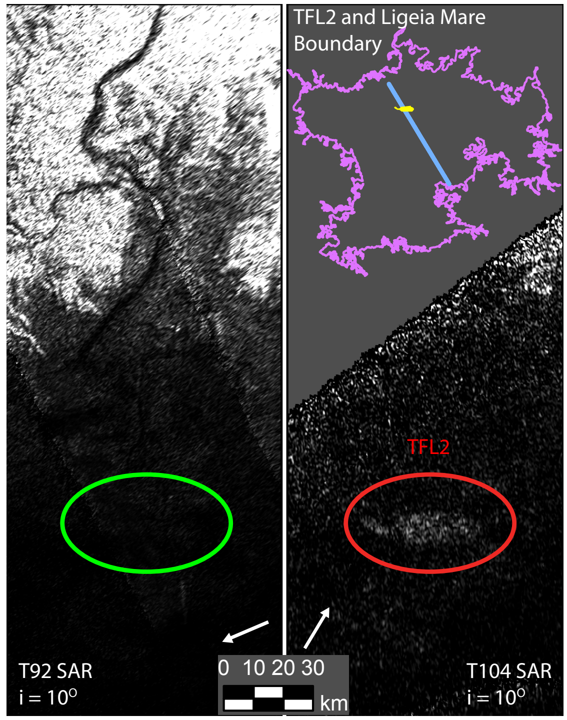

Figure 4.2: T92 and T104 observations of a part of Ligeia Mare that includes the region of TFL2. A transient bright feature, TFL2, is observed in the T104 observation (circled in red) that is not seen in any of the other observations of the region (the T25, T29, T64, T91, and T108 observations are shown in appendix B). The yellow region at the top of the right panel indicates the region of TFL2 within the purple boundary of Ligeia Mare and the blue line indicates the length of the transect that is shown in figure 4.5. Pixel brightness is linearly related to the normalized radar cross section. The white arrows indicate the radar azimuthal illumination directions and the subtitles provide the incidence angles.

TFL2 is also unlikely to be a SAR image artifact. It is not at the edge of a radar beam and is surrounded by dark pixels so it is unlikely to be an edge effect. Its brightness and distance from the shore/islands argues against range and azimuth ambiguities because the antenna pattern sharply reduces the backscattered energy from areas outside of the main lobe. Nadir ambiguities, scalloping, and gain control effects are unlikely to produce artifacts that are as spatially confined as TFL2 (Elachi and van Zyl, 2006).

4.3 Quantitative Constraints

4.3.1 TFL1

In this section, we derive quantitative constraints on TFL1 from the observations introduced in the previous section. Table 4.1 provides the average normalized radar cross section (NRCS) of the region of TFL1 in each radar image along with the most relevant observational parameters. The average NRCS of a region of Ligeia Mare and a region of land near to TFL1 are also included in the table. Other parameters for these two regions are included in appendix B. The region of TFL1-92 was defined as in Hofgartner et al. (2014) and this region was used to measure the NRCS for all of the observations except T104. The region of TFL1-104 was defined by a manual mapping of the anomalously bright region in the T104 image and is larger in area than TFL1-92 by greater than a factor of three. The results do not strongly depend on the definitions for the regions of TFL1-92 and TFL1-104 or on which of these two regions is used to measure the average NRCS for the other observations. The noise floors in table 4.1 are lower than in Hofgartner et al. (2014) because we have decreased the noise floors by increasing the number of independent measurements, assuming uncorrelated errors.

The dominant geometrical parameter for the Cassini RADAR measured NRCS of a permanent geophysical structure on Titan is the incidence angle of the observation. As the incidence angle decreases, more of the incident radar waves are backscattered to the spacecraft and the NRCS increases. The NRCS of the region of TFL1 is plotted as a function of incidence angle in figure 4.3. It is apparent that the observations of the region of TFL1 do not exhibit a mono-

Table 4.1: TFL1 quantitative constraints from each radar image and the most relevant observational parameters. 1 - Normalized Radar Cross Section; A negative NRCS is nonphysical. An estimate of the average noise floor is subtracted from the measured NRCS and statistical fluctuation of the noise floor can result in values slightly less than zero; 2 - One standard deviation; 3 - Clockwise from North; 4 - The Cassini Titan RADAR mapper transmits and receives in the same linear polarization and the polarization angle is defined as the angle between the electric field vector and the plane of incidence; 5 - Other parameters for this region are included in appendix B; 6 - Indicates TFL1 was not present; 7 - Indicates TFL1 was not observed but its presence is not known because it may not have been present or it may have been present but not detectable due to the high noise, high incidence angle combination of the observation.

	T25	T29	T64	T91	T92	T95	T104	T108
Date	02/22/07	04/26/07	12/27/09	05/23/13	07/10/13	10/14/13	08/21/14	01/11/15
TFL1 Area (km^2)	✗[6]	✗	✗	✗	39.5	?[7]	144.8	✗
NRCS[1] (linear)	-0.0170	-0.0015	0.0004	0.4654	0.5361	-0.0005	0.1281	0.0213
NRCS Uncertainty[2] (linear)	0.0051	0.0012	0.0003	0.1357	0.0222	0.0156	0.0039	0.0024
NRCS Noise Floor (linear)	0.0126	0.0020	0.0004	0.0019	0.0015	0.0769	0.0005	0.0004
Incidence Angle (^{O})	20.3	19.4	36.2	3.4	6.0	26.5	11.5	8.3
Azimuth Angle[3] (^{O})	84.3	37.7	243.6	99.6	262.4	201.7	80.3	235.3
Polarization Angle[4] (^{O})	56.2	81.9	88.1	85.6	89.7	23.7	46.6	84.8
Range Resolution (km)	1.08	0.51	0.27	2.50	1.36	3.00	1.11	1.00
Azimuth Resolution (km)	0.54	0.31	0.26	1.00	0.32	3.69	0.94	1.00
Titan True Anomaly (^{O})	16	15	71	69	68	68	246	245
NRCS of Nearby Region of Sea[5]	-0.0266	0.0031	0.0008	0.2530	0.0342	-0.0309	0.0144	0.0252
NRCS of Nearby Region of Land[5]	0.1798	0.2571	0.1576	1.8253	0.9058	0.1899	0.4411	0.5249

tonic increase in NRCS as the incidence angle decreases. This indicates that the backscatter is inconsistent with an unchanging geophysical structure and thus the region of TFL1 must have intrinsically changed. Quasi-specular models are frequently employed to describe the NRCS-incidence angle behavior at low incidence angles (ex. Wye (2011)). We have included the best-fit quasi-specular model in figure 4.3 but stress that this model clearly does not fit the measurements. Excluding the T92 and T104 measurements, the NRCS-incidence angle constraints are consistent with a monotonic, inverse correlation and the measured NRCS of these two anomalous observations is greater than would be predicted from a fit to the other observations. This is in agreement with the interpretation from the images in figure 4.1 that the region of TFL1 was intrinsically brighter during the T92 and T104 observations.

Other parameters of the imaging geometry that can affect the measured NRCS include the azimuth and polarization angles. The azimuth angles of the T92 and T104 observations (table 4.1) are nearly diametrically opposite, indicating that the appearance of TFL1 is not restricted to a particular azimuth of illumination. Furthermore, the azimuth angles of the T25 and T104 observations are nearly equal but TFL1 is only present in the latter. Thus it is unlikely that the azimuth angle of the observation is controlling the appearance of TFL1. Similarly, the distribution in the polarization angles suggests that this parameter also does not regulate the appearance of TFL1.

Figure 4.4 is a plot of the T91, T92, T104, and T108 NRCS profiles along the transect given by the blue line in the top panel of figure 4.1. The transect begins north of Ligeia Mare and crosses the sea, including the region of TFL1. The T91 profile has the greatest NRCS along the transect, consistent with its measurement at the smallest incidence angles. Similarly, the T92 profile is above the T104 profile because it was measured at more nadir incidence angles. The T108 profile crosses both the T92 and T104 profiles as the incidence angle of this

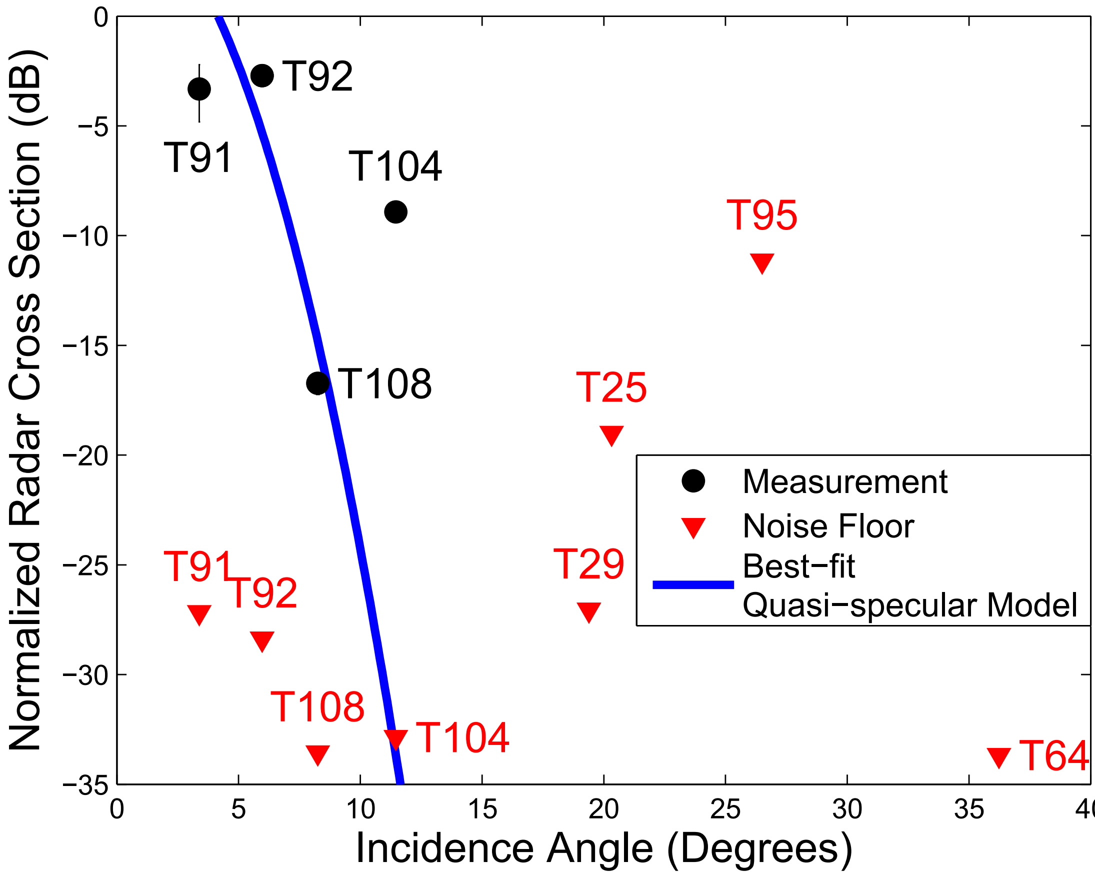

Figure 4.3: NRCS of the region of TFL1 as a function of incidence angle. The NRCS does not monotonically increase as the incidence angle decreases and the best-fit quasi-specular model poorly describes the NRCS-incidence angle behavior. Thus the backscatter is inconsistent with a permanent geophysical structure on Titan. The uncertainties of the T92, T104, and T108 NRCS measurements are included but are smaller than the size of their data points. The T25, T29, T64, and T95 measurements are not shown because they are below their respective noise floors.

observation increases along the transect, beginning smaller than that of the T92 observation and ending slightly larger than that of the T104 observation. The profiles are generally above their noise floors and where this is the case, they are also generally correlated with each other. This suggests that the measured NRCS is primarily from backscattering by the seafloor. Detection of the seabed of Ligeia Mare in RADAR observations has previously been demonstrated and the effective absorption of the sea was measured to be small (< 0.26 dB/m one way) (Mastrogiuseppe et al., 2014). In the region of TFL1 however, circled in red, there is a significant spike in the T92 and T104 profiles but no analogous spike in the T91 and T108 profiles. This supports our claim that TFL1 is present in the T92 and T104 observations but not the T91 and T108 observations. Also, with this context, we can now attribute the T91 and T108 measurements above the noise floor in the region of TFL1 as seabed signal. Furthermore, we note that the correlation of the T91 profile with the other profiles increases our confidence in the reliability of this observation despite its more speckled appearance in figure 4.1. The T29 profile is also included in the supplementary material of Hofgartner et al. (2014) (appendix A) but we have omitted it here to reduce clutter in the plot.

4.3.2 TFL2

A table and figure for TFL2, analogous to table 4.1 and figure 4.3 for TFL1, are included in appendix B to demonstrate that the NRCS-incidence angle behavior of TFL2 is also inconsistent with a permanent geophysical structure. Figure 4.5 is a plot of the T29, T91, T92, T104, and T108 NRCS profiles along the transect, given by the blue line in figure 4.2, that includes the region of TFL2. The profiles, like the profiles for TFL1 in figure 4.4, are generally above their noise floors and where this is the case, they are also generally correlated with each other, consistent with the interpretation that the backscatter is from the seafloor. In the region of TFL2 however, circled in red, there is a significant spike in the T104 profile but no comparable spike in any of the other profiles. Thus the region of TFL2 was likely intrinsically brighter during the T104 observation and we conclude that TFL2 is a second expression of an ephemeral phenomenon on

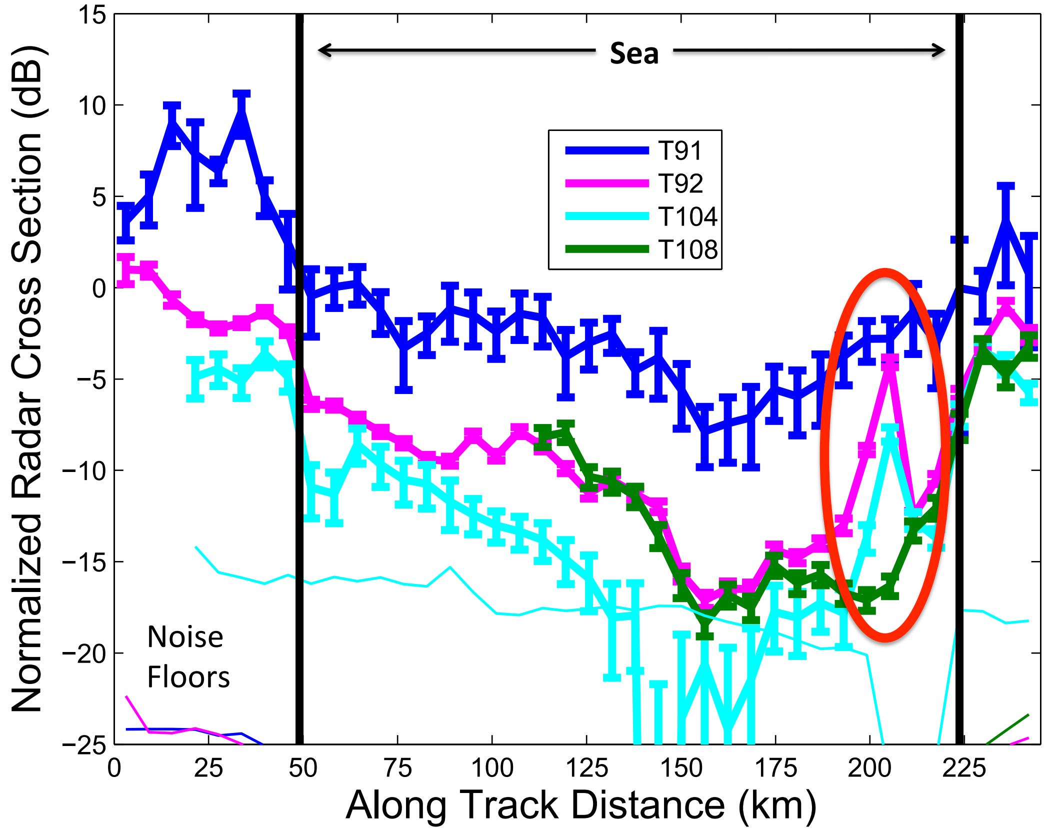

Figure 4.4: T91, T92, T104, and T108 NRCS profiles of a transect over Ligeia Mare that includes the region of TFL1. A large spike in the NRCS is apparent in the region of TFL1, circled in red, in the T92 and T104 observations but not the T91 and T108 observations. This indicates that TFL1 is only present in the T92 and T104 observations. Incidence angle varies from 3.3° to 3.5°, 4.6° to 6.2°, 14.8° to 9.8°, and 4.5° to 9.8° for the T91, T92, T104, and T108 profiles respectively. The long axis of the transect is indicated by the blue line in the top panel of figure 4.1 and the width is about 6 km.

Titan.

4.4 Transient Hypotheses

In this section, we use the observations and quantitative constraints in the previous two sections to assess hypotheses for the transient behavior of TFL1 and TFL2. We concentrate on TFL1 but note that since TFL2 has a similar NRCS at a

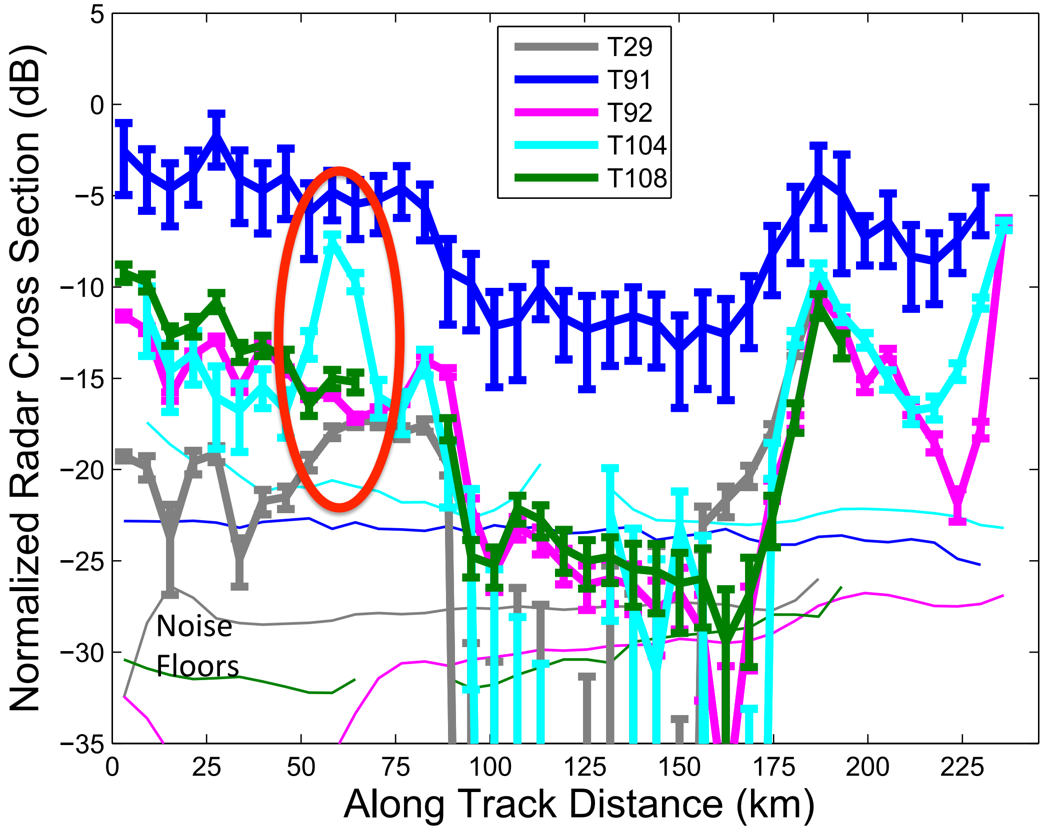

Figure 4.5: T29, T91, T92, T104, and T108 NRCS profiles of a transect over Ligeia Mare that includes the region of TFL2. A significant spike in the T104 observation is apparent in the region of TFL2, circled in red, but not the other observations. This indicates that TFL2 is only present in the T104 observation. Incidence angle varies from 22.2° to 15.7°, 3.8° to 4.2°, 9.3° to 10.9°, 11.5° to 7.6°, and 5.7° to 12.8° for the T29, T91, T92, T104, and T108 profiles respectively. The transect begins north of TFL2, its long axis is indicated by the blue line in figure 4.2 and its width is about 6 km.

similar incidence angle (0.126, 10.3°) to that of TFL1-104 (0.128, 11.5°), is in the same sea, and both regions were observed in the same high-resolution RADAR flybys, the assessments also apply to TFL2. As we have discussed, TFL1 is unlikely to be a SAR image artifact or permanent geophysical structure and thus its appearance is the result of an ephemeral phenomenon on Titan. We have not however distinguished if TFL1-92 and TFL1-104 are the detection of two separate occurrences of ephemeral phenomena or a single longer-lived ephemeral phenomenon.

4.4.1 Tides

Tidal forces from Titan's eccentric orbit around Saturn are predicted to generate dynamic behavior in its lakes and seas that could lead to time varying observable properties (Tokano et al., 2014). If TFL1 were an expression of tides, we would expect its presence to be a repeatable function of Titan's true anomaly. Table 4.1 includes the true anomaly of Titan relative to Saturn for each observation. The T64, T91, T92, and T95 observations were all at nearly the same true anomaly but TFL1 was only detected in the T92 observation, indicating that it is not the result of diurnal tides. Similarly, the T104 and T108 observations differed in their true anomaly by just one degree but TFL1 was only present in the T104 observation. Solar tides and tidal forces from Saturn's other moons are significantly weaker than the diurnal tides and unlikely to generate observable dynamic behavior in the lakes and seas.

4.4.2 Floating Solids

Floating solids are another phenomenon that could lead to the occurrence of transient bright features in Titan's liquids. Cassini RADAR observations combined with laboratory measurements constrain Ligeia Mare to be primarily composed of methane, ethane, and nitrogen (Mastrogiuseppe et al., 2014; Mitchell et al., 2015) and though all three components in their pure phases, have denser solids than liquids, solids formed from freezing of their liquid solutions may be buoyant (Roe and Grundy, 2012; Hofgartner and Lunine, 2013). If solutions of the solid and liquid phases coexist in equilibrium, they will differ in composition (sea ice on Earth is similarly less saline than the ocean from which it froze). Nitrogen, the densest of the three components, is more soluble in the liquid phase and the increase in density of this phase from nitrogen's increased abundance can make the coexisting solid phase positively buoyant. Aside from freezing of the liquid, solids may also occur in Titan's lakes and seas via several other plausible mechanisms including fluvial or aeolian delivery, mass wasting, and glacial calving. If the solids have a bulk density less than that of Ligeia Mare, such as possibly polyacetylene (Chien, 1984), they would float. Furthermore, solids of any composition could float in Ligeia Mare provided they have a sufficient porosity, until the pores fill with liquid, analogous to pumice rafts on Earth. To the authors' knowledge, these hypothetical floating solids have not been studied in detail and their radar scattering properties may occupy a large portion of phase space, so in this subsection we do not attempt to model all of these hypotheses but instead use a simple model to address the plausibility of the hypothesis of floating solids. We assume the NRCS of land near to TFL1 is representative of that of floating solids and use a nearby region of Ligeia Mare to characterize the NRCS of open sea. We consider the area of TFL1 as a linear mixture of floating solids (land) and sea and calculate the fraction of the area that must be filled with floating solids to reproduce the observed NRCS. In doing so, we are assuming that the area of TFL1 is not completely filled by a single floating solid but that portions of the area have sea at the surface which separates distinct patches of floating solids (or distinct exposures of floating solid), consistent with the knowledge that TFL1-92 is from multiple discrete features (Hofgartner et al., 2014). For the floating solids to have the same scattering behavior as the land, we are implicitly assuming that they are as dry as the land and have a minimum length of approximately ten radar wavelengths in all dimensions, to preserve surface slopes and volume scattering.

The NRCS of a region of land near TFL1 is plotted as a function of incidence angle in figure 4.6A using the parameters included in appendix B. The NRCS measurements are above their noise floors in all of the observations and follow the expected trend of decreasing as the incidence angle increases. This region of land does not appear to have temporally changed in either the images or its backscatter as shown in the NRCS-incidence plot. The best-fit combined quasi-specular plus diffuse model is also plotted and its parameters are given in the legend. This best-fit model will be the floating solids component of the linear mixture of floating solids and sea.

Figure 4.6: Linear mixing of floating solids (land) and sea. (A.) NRCS of a region of land near TFL1 as a function of incidence angle. The NRCS-incidence angle behavior is well described by the best-fit quasi-specular plus diffuse model and is consistent with a permanent geophysical structure on Titan. (B.) NRCS of a region of Ligeia Mare near to TFL1 as a function of incidence angle. With the exception of the T91 observation at the smallest incidence angle, the measurements are well described by the best-fit quasi-specular plus diffuse model. The model assumes the backscattering is from the seafloor and accounts for refraction and loss due to reflection at the atmosphere-sea interface but ignores absorption within the sea. The T91 observation was not included in the best-fit because it has a refracted incidence angle near a regime known to have anomalously large backscatter. The T25 and T95 measurements are not shown because they are below the lower limit of the plot. (C.) Linear mixing of floating solids (land) and sea. The NRCS of the region of TFL1 is plotted as a function of incidence angle along with the best-fit models from panels A. and B. The plot suggests the backscatter is primarily from the seafloor in all of the observations except T92 and T104 and these two observations are consistent with the presence of floating solids. The best-fit linear mixture of floating solids (land) and sea to the T92 and T104 observations is 57% and 30% floating solids respectively and the simultaneous best-fit to both observations is also plotted.

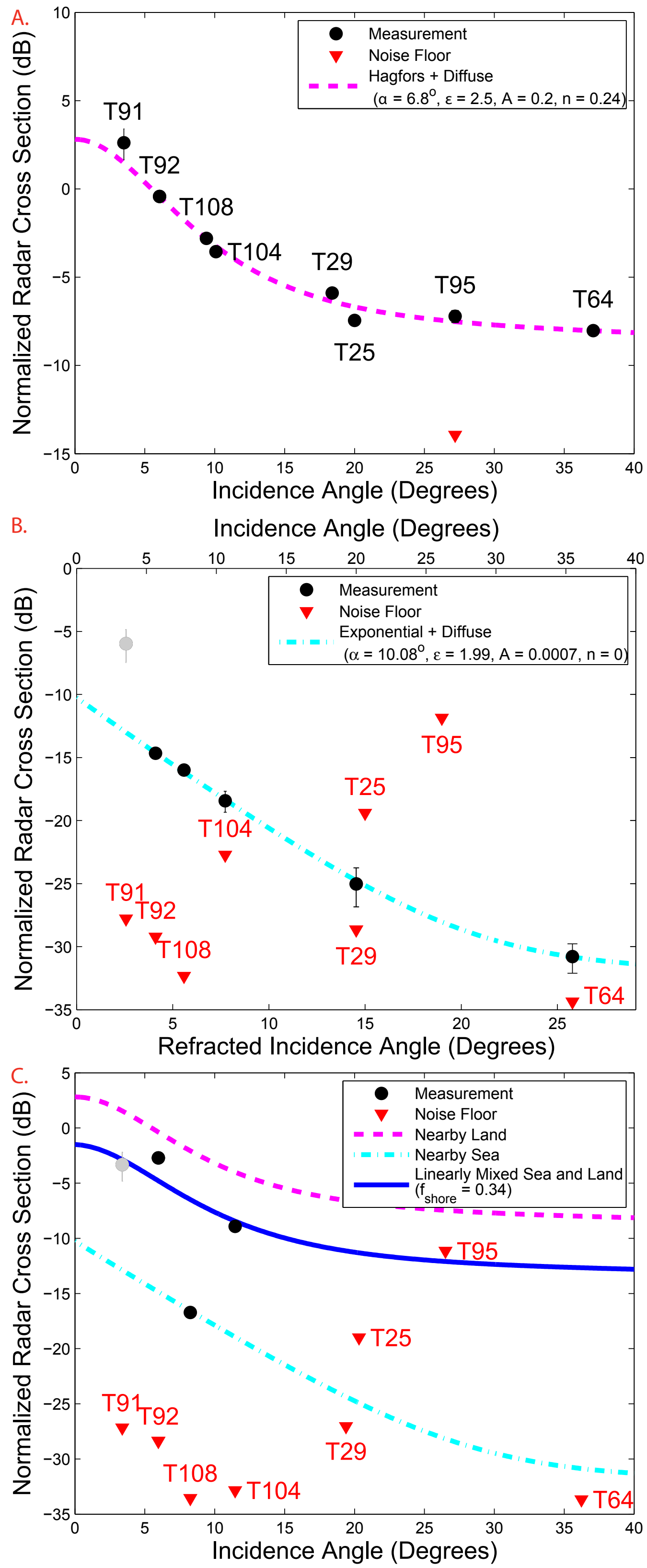

A.
Normalized Radar Cross Section (dB)
Incidence Angle (Degrees)
Measurement
Noise Floor
Hagfors + Diffuse
(α = 6.8°, ε = 2.5, A = 0.2, n = 0.24)
T91
T92
T108
T104
T29
T25
T95
T64
B.
Incidence Angle (Degrees)
Normalized Radar Cross Section (dB)
Refracted Incidence Angle (Degrees)
Measurement
Noise Floor
Exponential + Diffuse
(α = 10.08°, ε = 1.99, A = 0.0007, n = 0)
T95
T25
T104
T91
T92
T108
T29
T64
C.
Normalized Radar Cross Section (dB)
Incidence Angle (Degrees)
Measurement
Noise Floor
Nearby Land
Nearby Sea
Linearly Mixed Sea and Land
(f_shore = 0.34)
T95
T25
T91
T92
T29
T108
T104
T64

The NRCS of a region of Ligeia Mare near TFL1 is plotted as a function of incidence angle in figure 4.6B using the parameters included in appendix B. Most of the NRCS measurements are above their noise floors and all of these measurements follow the expected trend of decreasing as the incidence angle increases. These measurements are in agreement with our conclusion that the seafloor is likely the primary source for the measured backscatter of Ligeia Mare (figures 4.4 and 4.5). Refraction at the atmosphere-sea interface of the incident electromagnetic waves decreases their incidence angle and assuming a dielectric constant of 1.75 for Ligeia Mare (ϵ_{sea} = 1.75), the bottom x-axis of figure 4.6B is the refracted incidence angle (the top x-axis is the non-refracted incidence angle). Reflection at the atmosphere-sea interface while both entering and exiting the sea decreases the radar energy. For a perfectly smooth sea surface, a reasonable assumption away from the region of TFL1 (Zebker et al., 2014), the loss due to reflection can be calculated using the Fresnel reflection coefficients. Accounting for refraction and loss due to reflection, the best-fit combined quasi-specular plus diffuse model is also plotted in figure 4.6B. Scattering and absorption within the sea were ignored because the effective absorption of the radar energy by Ligeia Mare was measured to be small (Mastrogiuseppe et al., 2014) and including them introduces the depth as an additional variable in the model without significantly improving the fit (see the next subsection for an expanded discussion of absorption). We also ignored polarization in our calculations of the loss due to reflection, as all of the observations were at different polarizations (table 4.1) and accounting for it, changes the model NRCS by less than 1%. All of the observations, except for T91, can be well fit by a combined quasi-specular plus diffuse model. Titan terrains were measured to be anomalously bright at incidence angles of less than 2 degrees (Wye, 2011) and the refracted incidence angle of the T91 observation is 2.6 degrees. Thus we suspect the T91 NRCS may be anomalously large because of the small refraction-corrected incidence angle of the observation and have ignored this measurement in the best-fit. Excluding the T91 observation does not significantly affect the results of the linear mixing model. The effective reflectivity of the seafloor for the quasi-specular component of the model is determined by its dielectric contrast with the sea. For a Ligeia Mare dielectric constant of 1.75, a model with $\epsilon_{seafloor} = 1.54$ has the same effective reflectivity as the model with $\epsilon_{seafloor} = 1.99$ and thus fits the observations equally well. We expect however, that $\epsilon_{seafloor}$ is always greater than ϵ_{sea} since any pore spaces are probably liquid filled. We also point out that the numeric value of $\epsilon_{seafloor}$ is not representative of the true dielectric constant of the seafloor because ignoring absorption and scattering within the sea biases the model toward a dielectric constant that is nearer to that of the sea. The best-fit model in figure 4.6B will be the sea component of the linear mixture of sea and floating solids.

In figure 4.6C, as in figure 4.3, the NRCS of the region of TFL1 is plotted as a function of incidence angle. The best-fit quasi-specular plus diffuse model to the region of nearby open sea, from figure 4.6B, is also included. This model fits the T108 measurement and correctly plots below the noise floor of the T25 observation. This is consistent with the interpretation that TFL1 was not present at the time of these observations and the measured backscatter is primarily from the seafloor. For the T29 and T64 observations, the best-fit model for the open sea predicts the NRCS will slightly exceed the noise floor, which is inconsistent with the measurements. However the noise floors are so small that this discrepancy could be from a minor systematic error. For the T91 observation, the best-fit model predicts an NRCS that is three standard deviations less than the measured NRCS. We expect that this poor fit is because of the small refraction-corrected incidence angle of the observation, as discussed in the preceding paragraph. The model for the open sea does not fit the T92 and T104 observations because TFL1 was present at the time of these observations. The best-fit quasi-specular plus diffuse model to the nearby land, from figure 4.6A, is also plotted. Assuming TFL1 is a linear mixture of floating solids (land) and open sea, the simultaneous best-fit to the NRCS of TFL1-92 and TFL1-104 is 34% floating solids and this model is plotted in figure 4.6C. The best-fits to TFL1-92 and TFL1-104 individually are 57% and 30% floating solids respectively.

For the floating solids to backscatter like the nearby land, as has been assumed, they must be as dry as the land and have a minimum length of approximately ten radar wavelengths ($10\lambda = 0.216$ m) in all dimensions, to preserve surface slopes and volume scattering. The areas of ≈ 40 km^2 and ≈ 145 km^2 of TFL1-92 and TFL1-104 respectively (table 4.1) therefore imply volumes of floating solids greater than $\approx 5 \times 10^6$ m^3. If the floating solids originate from a single pixel of land in figure 4.1, the lower limit for the volume corresponds to a roughly 10 m thick layer. Thus if TFL1 is floating solids that originate from the land, the modification of the land may be undetectable. The modification of the land could also be undetectable for much larger volumes if the volume loss does not change the backscattering behavior. We therefore consider the hypothesis of floating solids for TFL1 as plausible.

Finally, we note that figure 4.6C also illustrates why the presence of TFL1 in the T95 observation is ambiguous. If the NRCS of TFL1 in the T92 and T104 observations is extrapolated to the incidence angle of the T95 observation, following typical functional behavior for Titan terrains (such as those of the nearby land), the predicted NRCS is similar to the noise floor of the observation. Thus the NRCS of TFL1 at the incidence angle of the T95 observation could be less than the noise floor of this observation, in which case, TFL1 would not have been detectable. It is therefore unclear if TFL1 was not detected in the T95 observation because it was not detectable, or not physically present.

4.4.3 Sea Level Change

A change in the liquid depth could lead to the appearance of transient features and has been documented to occur in Titan's south polar lakes during the southern summer season (Hayes et al., 2011; Turtle et al., 2011b). As we have discussed, the seafloor is likely the primary source for the measured backscatter of Ligeia Mare (figures 4.4, 4.5, and 4.6B), so a decrease in sea depth would reduce absorption by the sea and cause the seafloor to appear brighter. Absorption of the radar energy by the sea reduces the NRCS according to the following equation

$$\sigma^f = \sigma^i \exp(-\frac{2\pi}{\lambda}\sqrt{\epsilon_{sea}}\tan\Delta\frac{2z}{\cos i_{sea}}), \tag{4.1}$$

where σ^f and σ^i are the NRCS with and without absorption respectively, λ = 0.0216 m is the radar wavelength in vacuum, ϵ_{sea} is the real component of the dielectric constant of the sea, $\tan\Delta$ is the loss tangent of the sea, z is the sea depth and i_{sea} is the refracted incidence angle in the sea. Assuming a dielectric constant of 1.75, Mastrogiuseppe et al. (submitted) have measured the effective loss tangent of Ligeia Mare for the Cassini radar to be $4.4 \pm 0.9 \times 10^{-5}$ which corresponds to a decrease in the received signal of 0.14 ± 0.03 dB/m. The measured NRCS of the region of TFL1 in the T104 observation was greater than in the T108 observation despite a larger incidence angle (table 4.1). The decrease in absorption from a drop in sea level that would cause the observed brightening can be constrained by taking the ratio of equation 4.1 for the T104 and T108 observations. Upon evaluating and re-arranging, it can be shown that

$$z_{T108} - z_{T104} = 0.01 z_{T108} + 63 \text{ m} + \ln\left(\frac{\sigma^i_{T108}}{\sigma^i_{T104}}\right) 35 \text{ m}. \tag{4.2}$$

Now, $z_{T108} >= 0$ and since $i_{T108} < i_{T104}$, it is expected that $\sigma^i_{T108} > \sigma^i_{T104}$ and therefore the first and third terms on the right side of the equality are always greater than zero so $z_{T108} - z_{T104} >= 63$ m. Thus to explain the anomalous brightening in T104 through a decrease in absorption by a drop in sea level, the depth must have varied by more than 60 m. This large a change in sea level would be expected to result in significant and observable changes to the shoreline (unless it is very steep at all locations) and an increase in the measured NRCS of the seafloor in all regions of the sea, neither of which is observed and thus this hypothesis does not explain TFL1.

Aside from the decrease in absorption, a decrease in sea level could also increase the measured NRCS from exposure of the solid seafloor or a Titan analog of a guyot. If the seafloor is exposed to the atmosphere, the dielectric constant of the incident medium changes from that of the sea (about 1.75) to that of the atmosphere (approximately unity), which changes the effective Fresnel reflectivity. If the dielectric constant of the seafloor is similar to the dielectric constant of the sea, as it is for the best-fit model in figure 4.6B, exposure of the seafloor to the atmosphere increases the dielectric contrast and significantly increases the reflectivity. This change in the reflectivity is likely also partly the reason the boundary between the land and sea is so apparent in figures 4.1 and 4.2. As noted in the paragraph above, because $i_{T108} < i_{T104}$, if no temporal change had occurred we would have expected that $\sigma_{T104}/\sigma_{T108} < 1$. Since this NRCS ratio is greater than unity, to be consistent with these observations exposure of the seafloor must have increased the backscatter by at least a factor of $\sigma_{T104}/\sigma_{T108}$. Exposure of seafloor with $1.49 < \epsilon_{seafloor} < 2.55$ in the region of TFL1 is consistent with this increase, where the specific number depends upon the fractional area of change per SAR pixel. This range encompasses many of the materials expected at Titan's surface (Paillou et al., 2008). For the best-fit model of the seafloor (figure 4.6B), 66% of the region of TFL1-104 would have to be exposed in the T104 observation. As we discussed above however, significant shoreline changes are not observed here or elsewhere. Thus either the shoreline at all locations imaged in the T92 and T104 observations is much steeper than the seafloor in the region of TFL1 or the change in sea level was very small and the sea in the region of TFL1 was very shallow. The morphology required for either scenario seems ad hoc. Exposure from sea level change is a possible explanation for TFL1 but requires ad hoc assumptions and therefore is not favored.

4.4.4 Suspended Solids

The existence and transport of sediment at Titan's surface, including its marine environments, is well established as an integral component of its geology (Aharonson et al., 2014). Solid particles suspended within the volume of Ligeia Mare would backscatter the radar if their dielectric constant differed from that of the sea. The particles will act as Rayleigh scatterers if their radii are less than about ten percent of the radar wavelength (λ = 2.16 cm). The Cassini RADAR instrument transmits and receives in the same sense linear polarization and the NRCS of a single Rayleigh scatterer, σ_1, in this case is

$$\sigma_1 = \frac{16}{\pi}k^4 r^4 (\frac{\epsilon - \epsilon_{sea}}{\epsilon + 2\epsilon_{sea}})^2, \tag{4.3}$$

where k is the wavenumber, r is the particle radius, ϵ is the particle dielectric constant, and $\epsilon_{sea} = 1.75$ is the dielectric constant of the sea (Jackson, 1998). The scattering attenuates the energy of the incident radar beam by a factor of $1 - \alpha$, where

$$\alpha = \int \frac{\partial\sigma}{\partial\Omega}\partial\Omega = \frac{8}{3}k^4 r^4 (\frac{\epsilon - \epsilon_{sea}}{\epsilon + 2\epsilon_{sea}})^2. \tag{4.4}$$

Thus the effective NRCS of a second scatterer is $\sigma_2 = \sigma_1(1 - \alpha)$. For m scatterers along the line of sight, the total NRCS is

$$\sigma = \sum_{n=1}^{n=m} \sigma_1(1 - \alpha)^{n-1} = \frac{6}{\pi}(1 - (1 - \alpha)^m), \tag{4.5}$$

where multiple scattering has been ignored. The last equation indicates the NRCS of Rayleigh scatterers can range from $6\alpha/\pi = \sigma_1$ for $m = 1$, to a maximum of $6/\pi$ for $m \to \infty$. Reflection at the atmosphere-sea interface will reduce the effective NRCS by less than five percent. Figure 4.7 is a plot of the NRCS as a function of particle radius for different dielectric constants of the Rayleigh scatterers and different values of m. The NRCS of TFL1-92 and TFL1-104 are also included. If the particles are positioned such that they form a chain in the direction of the incident radar beam with no liquid between successive scatterers, for the maximum radius of $0.1\lambda, m = 10,000$ corresponds to ≈ 43 m thick stack. Since the maximum depth of Ligeia Mare is ≈ 160 m (Mastrogiuseppe et al., 2014), 10,000 is approximately the upper limit for m. Values of m much less than this upper limit however can be consistent with the observations. For particles with $r = 0.1\lambda$ and $\epsilon = 3$, $m = 22$ and $m = 4$ are consistent with TFL1-92 and TFL1-104 respectively.

A different model for the NRCS from volume scattering was presented in Zebker et al. (2008) where

$$\sigma = (1 - R)^2 2f \cos^n i. \tag{4.6}$$

In this equation, f is the fraction of power that escapes from the volume after penetration, n is the exponent of the cosine falloff for diffuse scatter, and i is the incidence angle. The factor $(1 - R)^2$ accounts for reflection at the atmosphere-sea interface as the radar signal enters and exits the sea and will reduce the effective NRCS by less than five percent. For small incidence angles, in the limit that $f \rightarrow 1, \sigma \approx 2$ in approximate agreement with the limit above of $6/\pi$. Therefore volume scattering, including Rayleigh scattering by particles within Ligeia Mare can be consistent with the measured NRCS of TFL1 and we consider suspended solids to be a plausible hypothesis.

4.4.5 Bubbles

Geologic, hydrologic, and biologic processes could conceivably generate transient bubbles in Ligeia Mare. Bubbles with radii of less than about ten percent of the radar wavelength would act as Rayleigh scatterers and have a dielectric constant slightly greater than unity. Figure 4.7 includes the NRCS from Rayleigh scatterers with $\epsilon = 1$ and from the figure it is apparent that bubbles can be consistent with the measured NRCS of TFL1. We therefore consider bubbles to also be a plausible hypothesis for TFL1.

4.4.6 Waves

At non-nadir incidence angles, rough surfaces backscatter more radar energy than smooth surfaces. A sea on Titan would therefore be brighter in Cassini SAR images when its surface is roughened by waves than when it is calm and

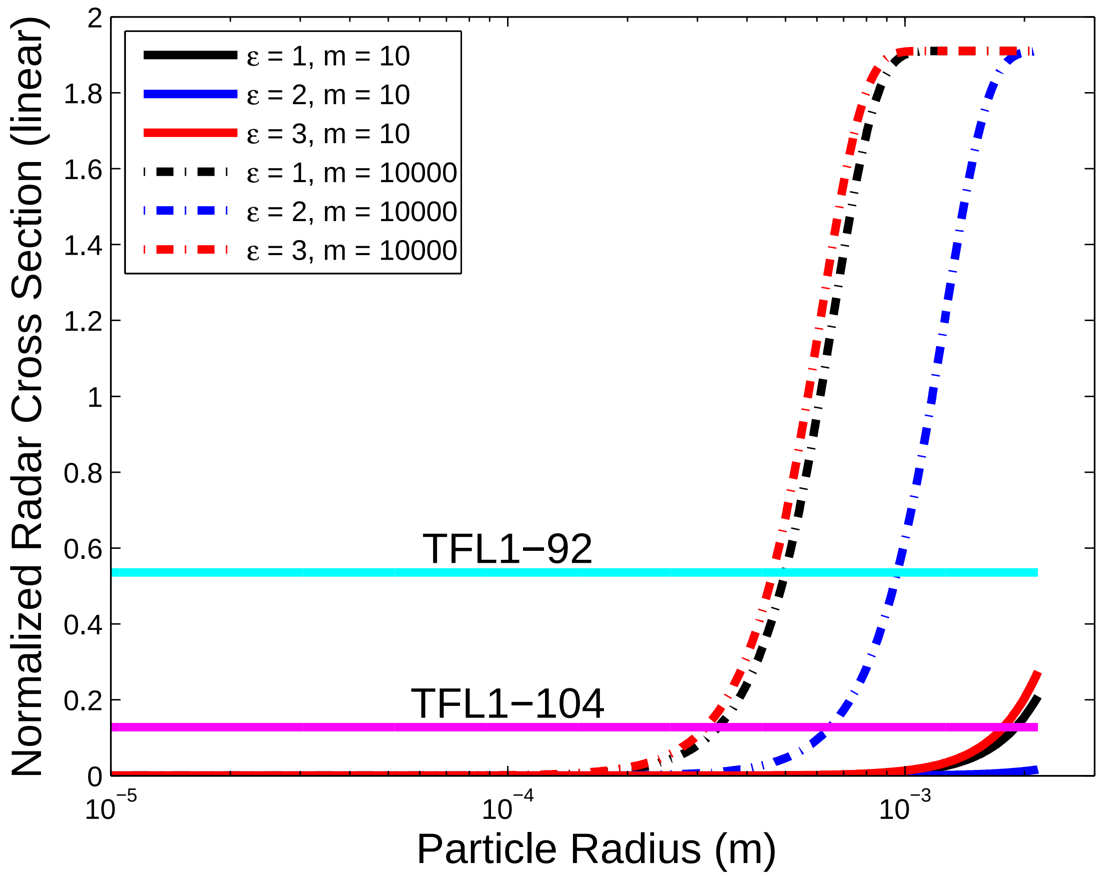

Figure 4.7: NRCS from Rayleigh scattering by suspended solids within Ligeia Mare as a function of scatterer radius. Multiple scattering is ignored, ϵ is the dielectric constant of the scatterers, and m is the number of scatterers in the direction of the incident radar beam. The NRCS ranges from 0 to $6/\pi$ and can be consistent with the measured NRCS of TFL1-92 and TFL1-104, indicating that TFL1 could be solids suspended within the volume of Ligeia Mare.

devoid of waves. The surface of a transect of Ligeia Mare was measured in the T91 observation to be extremely flat, with vertical deviations of only a few millimeters (Zebker et al., 2014), consistent with the dark appearance of the sea in SAR images (figure 4.1). Thus, here, we consider the hypothesis that TFL1 is a regional wave field on the sea during the T92 and T104 observations. Wind generation of capillary-gravity (cg) waves requires a minimum wind speed and wind speeds in Titan's north polar region are predicted by global circulation models to be below the threshold for wave generation, except in the spring and summer seasons (Hayes et al., 2013). The timing of the appearance of TFL1 is consistent with the forecasted onset of wind driven cg waves as Titan's 2017 northern summer solstice approaches (Hayes et al., 2013). TFL1 may have been absent during the T91 and T108 observations, during which, winds were also predicted to be near the threshold for wave generation, because of daily wind variability. On Earth, wind speeds near the threshold for wave generation are both more temporally and spatially variable (Shankaranarayanan and Donelan, 2001). Spatial variability of winds near the threshold for wave generation can result in regional wave fields and isolated bright patches are not uncommon in SAR images of terrestrial marine environments (ex. Jackson and Apel (2004)). Applied to Titan, this may explain the limited areal extent of TFL1 and funneling or deflection of wind by the topography of the nearby shoreline may explain its location.

The NRCS of wind driven cg waves on Titan's surface liquids was predicted by Hayes et al. (2013) by adapting the terrestrial model of Donelan and Pierson (1987) for the spectrum of wind generated cg waves and their microwave backscatter to the Titan environment. The backscatter is predicted using a two-scale model that includes both Bragg and quasi-specular scattering. The Bragg scattering component dominates the backscatter for incidence angles greater than about 15-25 degrees but is less important at smaller incidence angles. The backscatter model was developed for incidence angles greater than this transitionary regime and omits the Bragg scattering component for effective incidence angles of less than 18 degrees but the actual contribution to the backscatter may not be negligible. The Titan adapted model of Hayes et al. (2013) has not been observationally validated and thus we consider the NRCS predictions to be approximate. We evaluated this model at the incidence angles of the T92 and T104 observations and found that the predicted NRCS is always less than the measurements of TFL1, regardless of wind speed and liquid viscosity. The discrepancy between the model and measurements however is less than 5 dB for wind speeds greater than 1.4 m/s and we consider this to be agreement within the error of the model. Inclusion of the Bragg scattering component at the incidence angles of the T92 and T104 observations may reduce or eliminate the discrepancy but we leave this for future work. We also point out that a quasi-specular model where the prediction for the sophisticated wave spectrum is ignored and a Gaussian distributed surface is assumed is consistent with TFL1.

Other mechanisms for generating surface roughness, including currents flowing over obstacles, are also plausible. Tidal-, wind-, and density-driven currents are predicted to have a maximum speed of a few centimeters per second and thus, from energy balance, likely can only perturb the liquid surface topography by a few mm (Tokano et al., 2014; Tokano and Lorenz, 2015, in press). The currents however, are sensitive to the bathymetry and may be significantly faster in some regions, including regions with promontories like the peninsular shoreline near TFL1. Thus we consider waves to be a plausible hypothesis for TFL1.

4.4.7 Seafloor Change

Localized, ephemeral change of the seafloor is another phenomenon that could lead to the occurrence of transient bright features in Ligeia Mare. The seafloor is likely the primary source of the measured backscatter from Ligeia Mare and the best-fit quasi-specular plus diffuse model to a region of sea near to TFL1 is included in figure 4.6B. This model is also approximately consistent with the backscatter from the region of TFL1, except for the T92 and T104 observations when TFL1 was present, and is adopted as the base model for the backscattering from the seafloor in this region (figure 4.6C). TFL1-92 and TFL1-104 are consistent with an increase in the effective dielectric constant of the seafloor, ϵ, to approximately 2.7 or greater, where the specific number depends upon the observation, the change of the seafloor roughness parameter, α, and the fractional area of change per SAR pixel. We expect that ϵ is always greater than the dielectric constant of the sea (ϵ_{sea} = 1.75) since any pore spaces are probably liquid filled but for completeness we point out that a decrease of ϵ to approximately 1.2 or less is also consistent with the NRCS of TFL1-92 and TFL1-104. We also point out that absorption and scattering within the sea were ignored in the best-fit model and this biases ϵ toward a dielectric constant that is nearer to that of the sea. While a change of ϵ alone can be consistent with the NRCS of TFL1, a change of solely the roughness parameter, α, cannot. At the incidence angles of the T92 and T104 observations, the backscatter from Titan's solid terrains is generally dominated by the quasi-specular component. However we note that TFL1-92 and TFL1-104 are also consistent with an increase in the amplitude of the diffuse component, A, by factors of approximately 700 and 100 or greater. A change of the diffuse n-coefficient alone is not consistent with either TFL1-92 or TFL1-104. Thus if TFL1 is an expression of seafloor change, the change must have included an increase in the dielectric constant or diffuse amplitude. Possible mechanisms for increasing the effective dielectric constant of the seafloor include removal of sediment and exposure of an underlying surface or mantling with a different material. Dielectric constants greater than 2.7 are consistent with some other Titan terrains (Wye, 2011) and some of the materials expected at Titan's surface (Paillou et al., 2008). The amplitude of the diffuse backscattering could increase if the volume scattering, dielectric constant, or small-scale roughness increase.

If seafloor change occurred in the region of TFL1, the absence of anomalously bright features in the T108 observation (figure 4.1), lack of spike in the T108 NRCS profile (figure 4.4), and agreement of the seafloor model with the T108 NRCS (figure 4.6C), all suggest that the seafloor had reverted back to its base state by this observation. Reversion of the seafloor is likely neither an inevitable nor highly probable outcome of processes that may cause seafloor change and thus, in our view, is ad hoc. Therefore it is possible that TFL1 is an expression of seafloor change but we do not favor this hypothesis.

4.5 Discussion

Seven transient hypotheses for TFL1 have been considered. The focus was on the phenomenon rather than the underlying physical mechanism behind the phenomenon, as multiple mechanisms for each phenomenon are plausible and not distinguishable with the available data. TFL1 is unlikely to be an expression of tides because its presence is not a repeatable function of Titan's true anomaly as would be expected. Two hypotheses, sea level change and seafloor change, can be consistent with the measured NRCS but require ad hoc assumptions and are therefore considered as possible but not favored. For both of these hypotheses, TFL1 is the observation of an outcome of an ephemeral phenomenon rather than observation of the ephemeral phenomenon as it is occurring. If TFL1 is an observation of a process while it is occurring, reversion is expected when the process ceases but reversion is not necessarily predicted in the case of an outcome. Thus the absence of TFL1 in the most recent observation requires at least one additional assumption for the sea level change and seafloor change hypotheses. The remaining four hypotheses, floating and suspended solids, bubbles, and waves are our favored hypotheses. We are not able to determine from the observations and quantitative constraints which of these hypothesized ephemeral phenomenon is responsible for TFL1. The time interval between the T92 and T104 observations is greater than 13 months, thus if the predicted currents of Tokano et al. (2014); Tokano and Lorenz (2015, in press) are correct, this suggests TFL1-92 and TFL1-104 are separate events. If we consider the frequency of each of these phenomena per unit area on liquid water bodies on Earth, waves occur at a much higher frequency than the other phenomena. From this terrestrial context we therefore consider waves to be the most likely explanation of TFL1. The same conclusions also apply to TFL2 because of its similarity to TFL1-104.

Increased solar insolation as Titan approaches its 2017 northern summer solstice was predicted to lead to the onset of dynamic phenomena (Hofgartner and Lunine, 2013; Hayes et al., 2013; Tokano and Lorenz, 2015, in press). The appearance of TFL1 in the T92 observation, halfway between the vernal equinox and summer solstice and its presence along with TFL2 in the later T104 observation, are consistent with this expectation. Isolated rough patches in Punga Mare during the T85 observation, also most likely from waves, have similarly been interpreted as indicative of the changing seasons (Barnes et al., 2014). However the absence of TFL1/TFL2 in the T91 and T108 observations, which were also in the spring season, weakens the seasonal correlation. Large scale and frequent cloud outbursts in the north polar region were also predicted to accompany the approach to solstice (Schneider et al., 2012) but have thus far not been observed. Future observations may improve the statistics and allow for rejection or confirmation of the association of TFL1/TFL2 to the changing seasons.

Some mechanisms for the most likely transient hypotheses involve meteorological phenomena. The Cassini Imaging Science Subsystem (ISS) did not observe clouds in the vicinity of Ligeia Mare during the T92 and T104 observations but the observations were unfavorable for the detection of clouds and thus cannot constrain the presence of clouds smaller than approximately 100 km, much larger than the size of TFL1/TFL2. The VIMS and ISS instruments have observed regional clouds of this size during the spring season. Thus we cannot constrain the role of meteorology on TFL1/TFL2.

The shore nearest to the region of TFL1 as shown in the lower panels of figure 4.1, appears to be more peninsular and reminiscent of a fjord morphology than other sections of Ligeia Mare's shore. This land mass also protrudes further toward the center and darkest part of the sea than most other segments of the shoreline. This unique shoreline could funnel or deflect winds and currents and/or result in increased erosion and geologic activity and thus may be related to TFL1. TFL2 by contrast is more than 50 km from its nearest shore/island. The wide, liquid-filled valley shown in the left panel of figure 4.2 however appears to continue as a submarine valley with a terminus near to the region of TFL2. Thus the region of TFL2 may be the sink for sediment that propagates down the valley and/or the boundary between river and sea dominated regions. Backscatter changes in parts of Moray Sinus, an estuary of Kraken Mare may be similarly associated with its nearby valleys (Hayes et al., 2011). Future observations could better constrain the association of dynamic phenomena in Titan's liquids to shoreline features.

There is only one remaining planned Cassini RADAR close flyby of Titan's north polar region before the end of the mission. If the regions of TFL1/TFL2 or other areas of Titan's lakes and seas are observed during the T126 flyby in April 2017, the results may further illuminate the ephemeral phenomenon responsible for TFL1/TFL2. The Cassini ISS and VIMS instruments also plan to observe Titan's north polar region in the future and these observations may also be revealing. Titan's hydrocarbon liquids are practically transparent at microwave wavelengths (Mastrogiuseppe et al., 2014; Mitchell et al., 2015) but much more opaque at near-infrared wavelengths (Clark et al., 2010). Thus detection of TFL1/TFL2 or similar transient features by the RADAR instrument along with near-coincident observation by the ISS/VIMS instruments may constrain whether the transient features are located on or beneath the liquid surface. It is possible however that the next observation of transient features in Titan's liquid environments may have to wait until there is a vessel on one of its seas. (Stofan et al., 2013).

4.6 Conclusions

The region of Titan's hydrocarbon sea, Ligeia Mare, where transient bright features (TFL1) had previously been discovered (Hofgartner et al., 2014), was anomalously bright in the first (T104) of two new Cassini RADAR observations but not the second (T108). A second transient bright feature in Ligeia Mare (TFL2) was also discovered in the T104 observation. TFL1 and TFL2 are unlikely to be SAR image artifacts or permanent geophysical structures and thus their appearance is the result of an ephemeral phenomenon on Titan. Floating and suspended solids, bubbles, and waves are favored hypotheses over tides, sea level change and seafloor change, in agreement with the conclusions of Hofgartner et al. (2014). We favor waves as the most probable explanation for TFL1/TFL2 because of their increased frequency over floating and suspended solids and bubbles in analogous terrestrial settings. TFL1 is the first confirmed instance of active processes in Titan's lakes and seas and together with TFL2 demonstrates that Titan's seas are not stagnant but rather dynamic environments.

Acknowledgements

J.D.H. gratefully acknowledges the Cassini RADAR and VIMS Teams for the data and the opportunity to lead the analysis and the Natural Sciences and Engineering Research Council of Canada, Post Graduate Scholarship program and Cassini Project for financial support. J.I.L. thanks the Cassini Project for support. A.G.H. and M.M. acknowledge support from NASA grants NNX14AJ57G and NNX13AG03G. We sincerely thank all attendees of the Lakefest and Titan Surface Workshops at Cornell University for very helpful discussions that improved this work.

APPENDIX A

SUPPLEMENTARY MATERIAL FOR CHAPTER 3

A.1 Morphology

The left panel of figure A.1 is a higher-zoom image than in figure 3.1 of the anomalous features in the T92 observation. The right panel is the same image with red crosshairs, centered on the locally brightest pixels, that have long and short axes given by the range and Doppler resolutions (1.36 km and 0.32 km) respectively of the T92 observation. Some of the crosshairs are separated by several resolution elements of dark pixels, suggesting that the intervening pixels correspond to the sea. Thus the anomalous, bright backscatter is likely not from a single contiguous structure but rather from distinct features, hence the reason for our use of the plural when referring to them. We note however that each crosshair should not be interpreted as corresponding to a distinct feature (the narrow dark strips sandwiched between crosshairs are consistent with the low values in the distribution of the measured NRCS), only regions separated by several resolution elements of dark sea-pixels are interpreted as distinct features. Some of the anomalies were larger than the T92 resolution element and some may have been smaller. From the figure, it is also apparent that the elongation of the components in the range direction (approximately east-west) is due to the resolution of the image and thus doesn't necessarily reflect the actual morphology.

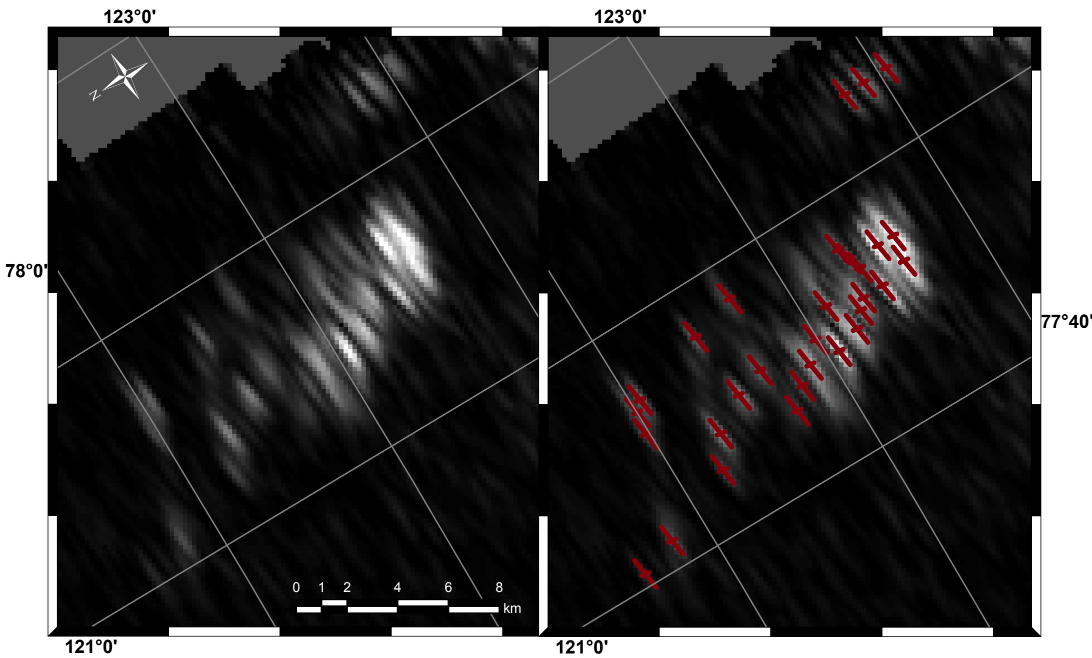

Figure A.1: The left panel is a higher-zoom image than in figure 3.1 of the anomalous features in the T92 observation. The right panel is the same image with red crosshairs, centered on the locally brightest pixels, that have long and short axes given by the range and Doppler resolutions (1.36 km and 0.32 km) respectively of the T92 observation.

A.2 Examination of Possible SAR Artifacts

Here, we examine the T92 image for possible SAR artifacts that could correspond to the anomalous bright features. There are two types of artifacts in SAR imagery that could produce small, localized, bright features: ambiguities and edge effects (Elachi and van Zyl, 2006). We argue below that the anomalous bright features observed in the T92 observation are unlikely to be artifacts of either type.

A SAR image is constructed by partitioning a radar echo (backscattered energy) into distinct time delay and Doppler shift bins (Elachi and van Zyl, 2006). The viewing geometry of the sensor is designed such that the equi-delay and equi-Doppler lines on the surface of the target body (Titan) are approximately perpendicular. Thus partitioning the radar echo by both time delay and Doppler shift results in a two dimensional image. To form the image, the radar echo is assumed to have a periodic waveform with a period given by the radar pulse repetition interval (t_0). As a result of this assumption, time delay bins that are separated by an integer multiple of t_0 cannot be distinguished. Similarly, Doppler shift bins separated by an integer multiple of the pulse repetition frequency ($f_0 = 1/t_0$) also cannot be distinguished. For integers k and n, a particular pixel in a SAR image may be contaminated by bright structures that are kt_0 removed in time delay (range ambiguities) and/or nf_0 removed in Doppler shift (azimuth ambiguities). To avoid these ambiguities, imaging radars use directional antennas with gain patterns that restrict a received echo to be dominated by the backscatter from a confined region of the surface. For the T92 observation, at the location of the anomalies, the antenna gain pattern reduced the echo energy from all ambiguous regions by greater than a factor of 100. The brightness of the anomalous features implies that if they are a SAR ambiguity, they correspond to a very bright source. Indeed, the hypothetical ambiguous source would have had an NRCS of > 10 dB, brighter than any non-nadir (0 degrees incidence) echo previously observed on Titan. The time delay and Doppler shift bins for the anomalous signal are not an integer multiple of t_0 or f_0 from nadir respectively, indicating that this signal is not from a nadir ambiguity. Edge effects are errors that occur in the parts of the image that map near the edge of the antenna gain pattern. These artifacts are typically bright or dark lines along an edge of the antenna pattern. As seen in figures A.2-A.4, the anomalous region was not on an edge of the T92 antenna pattern.

Cassini SAR observations utilize five different feeds that have antenna gain patterns in different directions (Elachi et al., 2004). As Cassini passes over Titan, each feed obtains multiple images in the along-track direction. Since these images overlap, each bin is imaged multiple times and when combined, they form a multi-looked image that extends the length of the flyby. The images formed from each feed are combined in the time delay dimension to construct the full-width SAR strip. Figure A.2 is a portion of the extended, multi-looked T92 SAR image formed from the fifth feed. The parallelogram shaped area between the two green arrows corresponds to the region illuminated by the main lobe of the antenna gain pattern of the fifth feed. The received waveform was processed for areas far enough away from this region to include this region's range ambiguities. The bright, distorted region on the left of figure A.2 is the energy from the main lobe of the fifth feed misplaced to a zone that is t_0 removed in time delay. This zone appears brighter than the parallelogram region because during SAR processing the measured power is divided by the antenna gain and the antenna gain for this zone is smaller. We see that the range ambiguity separation is much larger than the width of the main lobe of the antenna pattern and that the antenna pattern sharply cuts off the return from areas outside of the main lobe. Thus it is unlikely that the anomalous bright features are a range ambiguity. In figure A.3, the image constructed from the fifth feed (top panel) is compared to the image constructed from all five feeds (bottom panel). From the figure, it appears that no energy is received by the fifth feed from the bright structures within the red box. That the antenna pattern adequately reduces the energy received from these nearby, bright structures implies that it is also likely to sufficiently reduce the received energy from the more distant regions that could correspond to range ambiguities, where the antenna gain is even lower. This provides greater confidence that the anomalous signal is not the result of a range ambiguity. Figures A.2 and A.3 also show that the anomalous bright region is unlikely to be an edge effect because the closest edge of the antenna pattern is well to the right of the anomalous region. The peninsula that is closer to the edge than the anomalous features has been observed previously and does not exhibit any noticeable edge effects in the T92 observation.

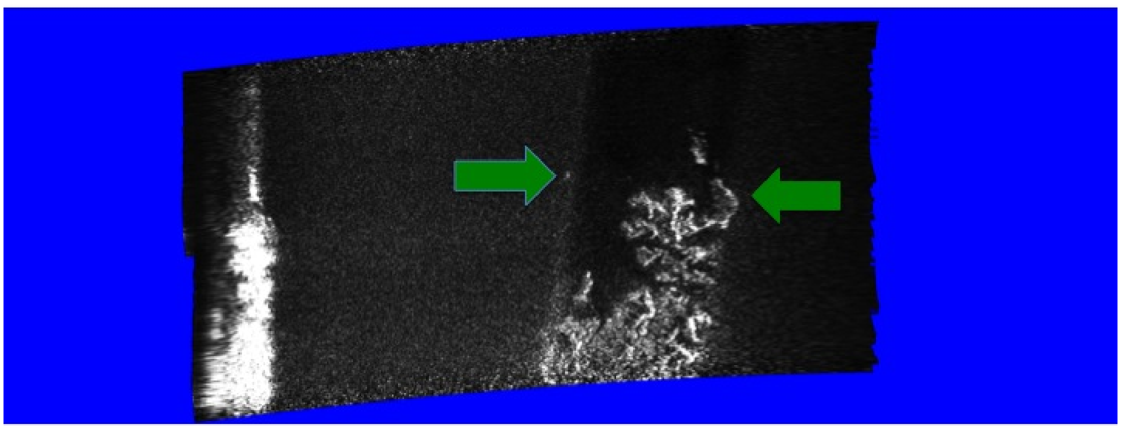

Figure A.2: Multi-looked T92 SAR image from antenna feed 5. The parallelogram shaped area between the two green arrows indicates the extent of the main lobe of the antenna gain pattern and includes the region of the anomalous features. The bright zone on the far left is the range ambiguity obtained by misplacing the entire echo by one pulse repetition interval, t_0, in the time delay dimension.

To investigate azimuth ambiguities we constructed separate images from

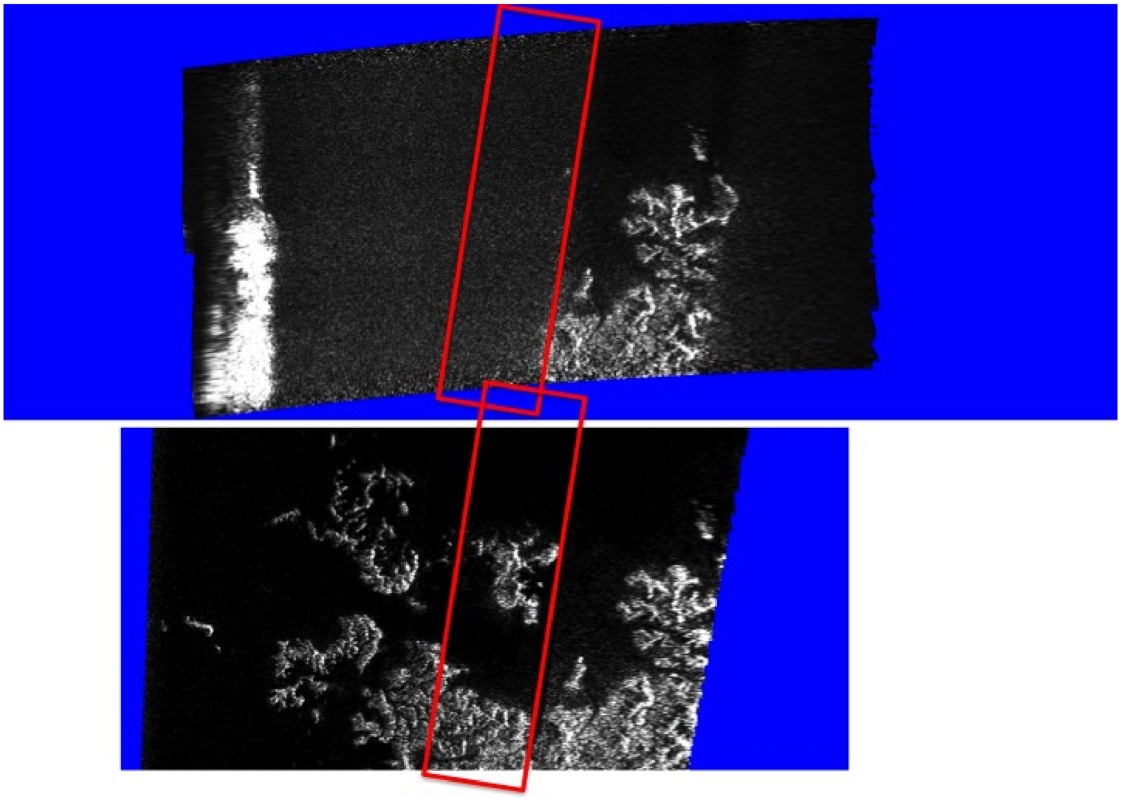

Figure A.3: Multi-looked T92 SAR image from antenna feed 5 (top panel) compared to the image constructed from all five feeds (bottom panel). Bright structures inside the red box, just outside of the main lobe of the fifth feed are adequately reduced by its antenna gain pattern. The range ambiguities, further to the left, where the gain reduction is even stronger are unlikely to explain the anomalous features.

each look of the region of the anomalous features. The top panels of supplementary figure A.4 are the sequence of single-look T92 images of the anomalous bright region. The bottom panel is the image formed from combining these images. We note that the anomalous features move within the antenna pattern as Cassini passes by but are approximately constant in brightness. This behavior is consistent with observations of real geophysical, bright structures. Azimuth ambiguities however, tend to result in bright features near the edge of the antenna pattern (left and right of the images in the top panels) that darken as they move toward the middle because they are divided by the increasing antenna gain during calibration. Thus it is unlikely that the anomalously bright features are an azimuth ambiguity.

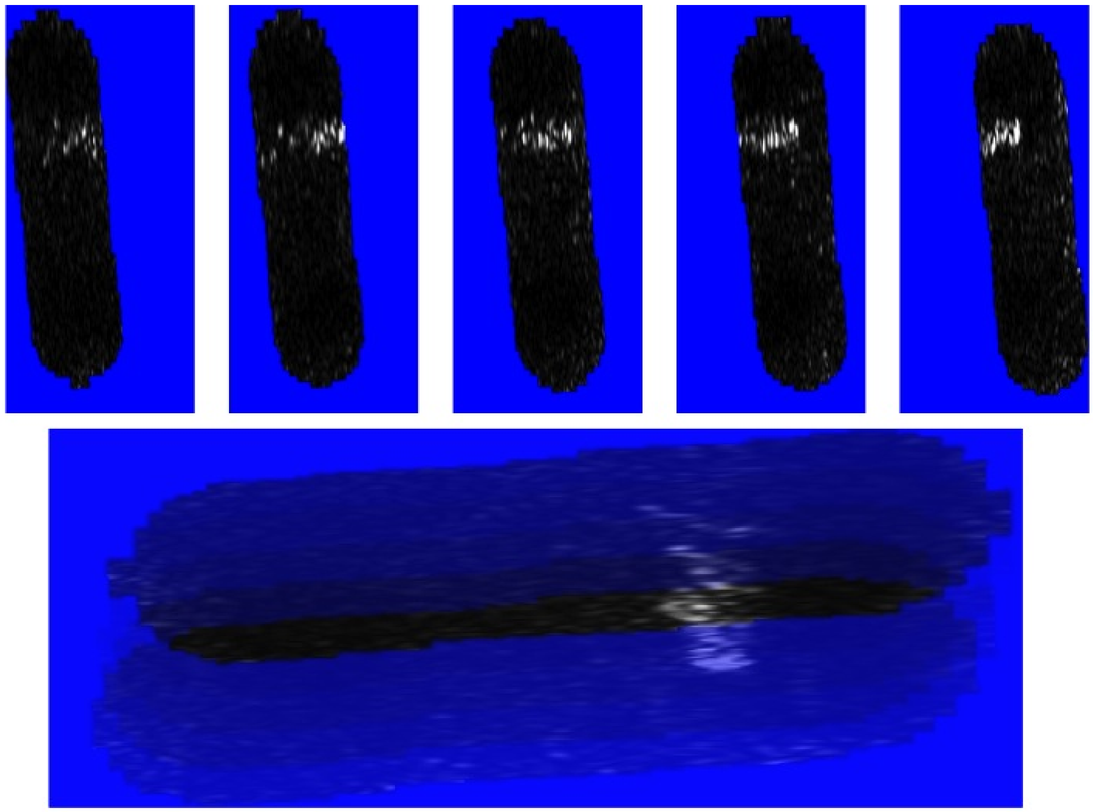

Figure A.4: The top panels are time-ordered, single-look T92 images of the anomalous features and the bottom panel is their combined multi-look image. The images in the top panel are rotated by 90 degrees with respect to the images in figures A.2 and A.3 and the bottom panel. The consistent brightness of the anomalous features in the images indicates that they are unlikely to be the result of an azimuth ambiguity.

A.3 T91 Image

We present additional arguments here to support our claim that despite the noticeably greater speckle noise in the T91 image compared to the other radar images, it still contains credible signal.

We repeated the incidence angle analysis on one of the nearby peninsulas that are visible toward the lower right in the zoom-panels of figure 3.1. Figure A.5 is a plot of the NRCS of the peninsula as a function of incidence angle. As expected for a permanent, static structure and consistent with all major terrain classes on Titan, the NRCS of the peninsula is well fit by quasi-specular plus diffuse scattering models (Wye et al., 2007; Wye, 2011). The best-fit models are also plotted in the figure and their parameters are given in the legend. These parameters are similar to the parameters that others have measured for Titan terrains (Wye et al., 2007; Wye, 2011). This result gives us confidence that the signal in the T91 image is valid. That the NRCS of the peninsula increases as incidence angle decreases from 6 to 3 degrees indicates that the unexpected NRCS behavior of the anomalous features is likely not due to a bias introduced in the analysis.

Figure A.6 is identical to figure 3.3 of the main manuscript with the exception that it also includes the T29 profile. The T29 profile is also approximately correlated with the T91 and T92 profiles. These three profiles constitute all of the passes that completely covered the region of the transect.

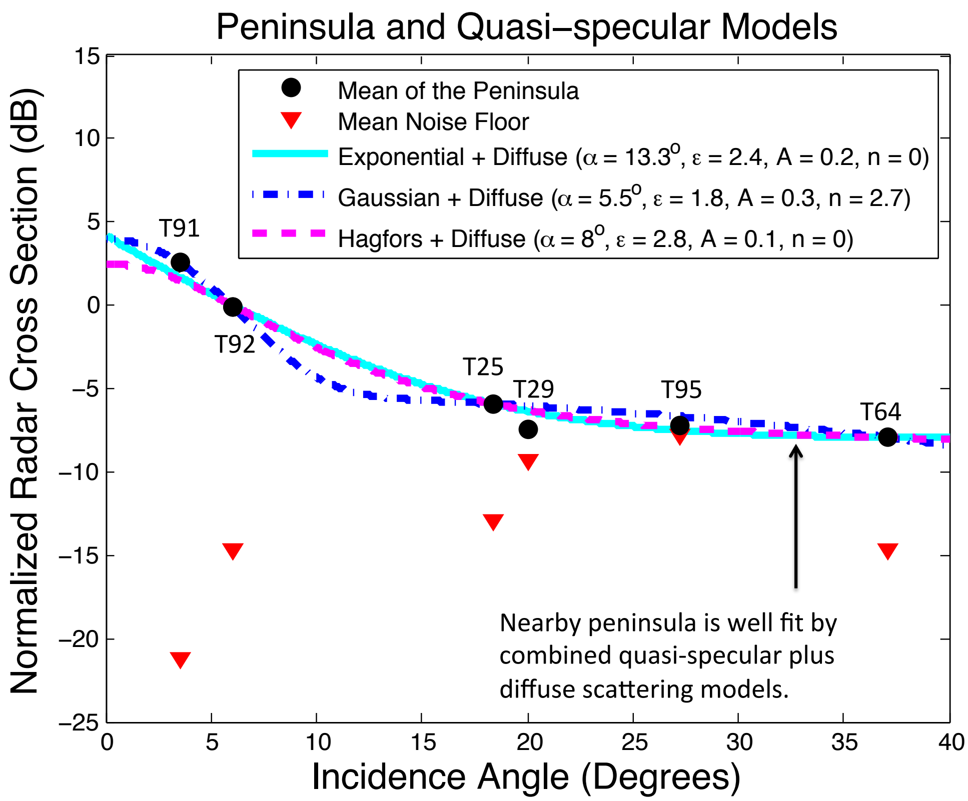

Figure A.5: Normalized radar cross section as a function of incidence angle of a peninsula near the anomalous features. The best-fit quasi-specular plus diffuse scattering models for the peninsula are also plotted and their parameters are given in the legend. The error bars show the one-sigma confidence.

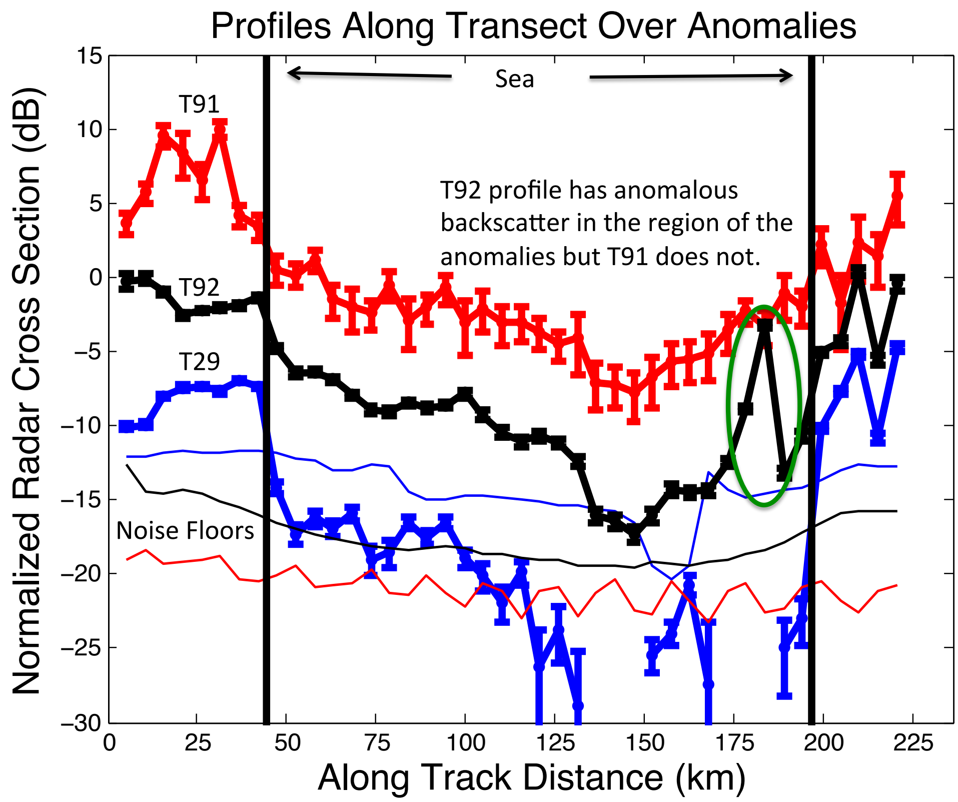

Figure A.6: Normalized radar cross section profiles along a transect of Titan that crosses Ligeia Mare including the region of the anomalous features. The correlation of the profiles suggests that the signal in the T91 image is valid. In the region of the anomalous features, the T92 profile exhibits a large spike (circled in green) but no similar anomalous spike is observed in the T29 and T91 profiles. The incidence angle along the transect varies from 26.7° to 17.9°, 3.3° to 3.5°, and 4.6° to 6.2° for the T29, T91, and T92 observations respectively. The blue line in figure 3.1 indicates the center of the transect. The error bars show the one-sigma confidence.

APPENDIX B

SUPPLEMENTARY MATERIAL FOR CHAPTER 4

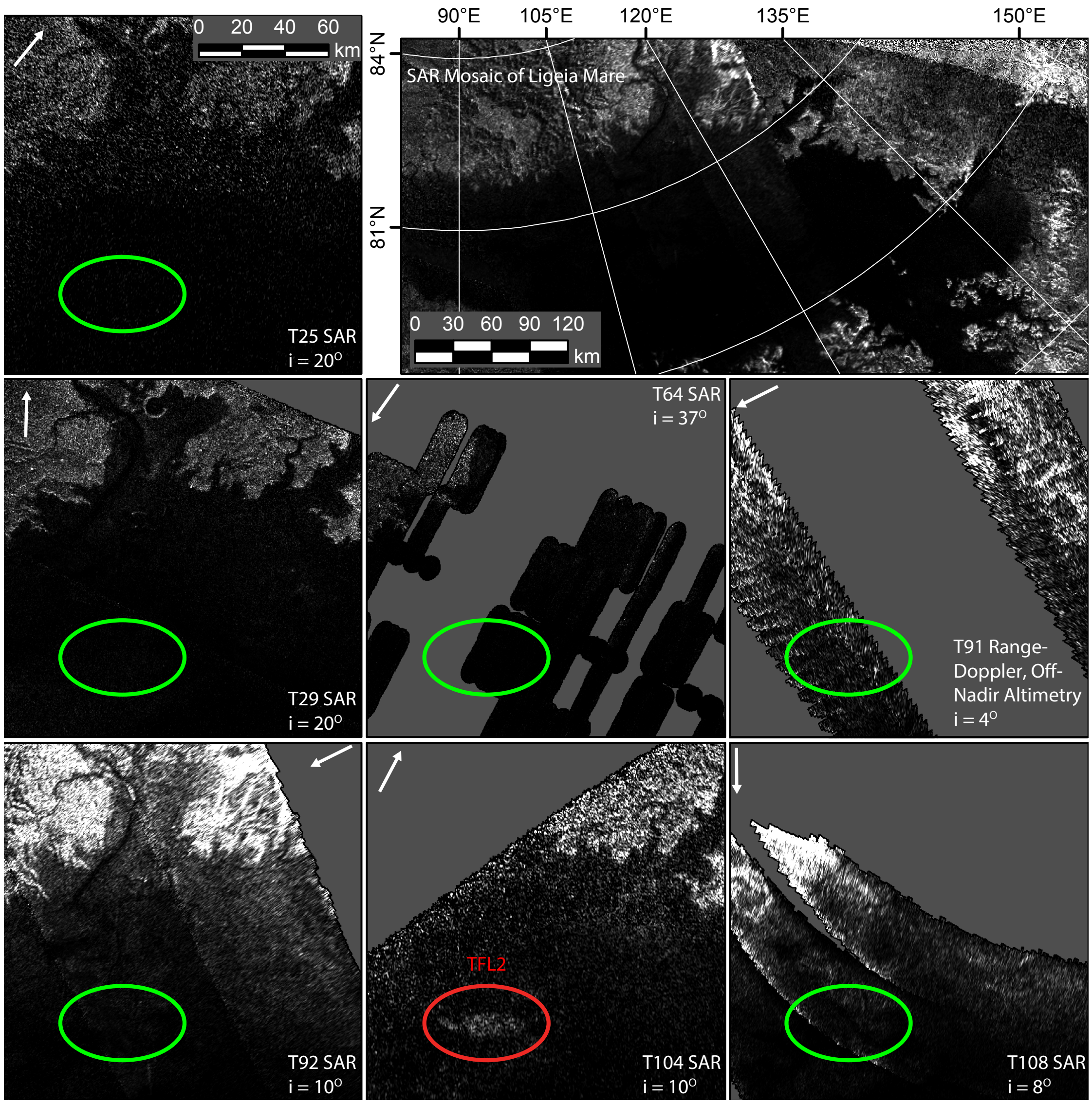

Figure B.1: Titan's Ligeia Mare and all high-resolution observations of the region of TFL2. A transient bright feature, TFL2, is observed in the T104 observation (circled in red) that is not seen in any of the other observations. Pixel brightness is linearly related to the normalized radar cross section. The white arrows indicate the radar azimuthal illumination directions and the subtitles provide the incidence angles.

Table B.1: Quantitative constraints of a region of Ligeia Mare near to TFL1 from each radar image and the most relevant observational parameters. The area of the region is 52.4 km^2. 1 - Normalized Radar Cross Section; A negative NRCS is nonphysical. An estimate of the average noise floor is subtracted from the measured NRCS and statistical fluctuation of the noise floor can result in values slightly less than zero; 2 - One standard deviation; 3 - Clockwise from North; 4 - The Cassini Titan RADAR mapper transmits and receives in the same linear polarization and the polarization angle is defined as the angle between the electric field vector and the plane of incidence.

	T25	T29	T64	T91	T92	T95	T104	T108
Date	02/22/07	04/26/07	12/27/09	05/23/13	07/10/13	10/14/13	08/21/14	01/11/15
NRCS[1] (linear)	-0.0266	0.0031	0.0008	0.2530	0.0342	-0.0309	0.0144	0.0252
NRCS Uncertainty[2] (linear)	0.0046	0.0011	0.0002	0.0733	0.0020	0.0134	0.0027	0.0022
NRCS Noise Floor (linear)	0.0115	0.0014	0.0004	0.0017	0.0012	0.0651	0.0053	0.0006
Incidence Angle (^{O})	20.6	20.0	35.5	3.5	5.6	26.1	10.6	7.7
Azimuth Angle[3] (^{O})	83.4	58.1	241.6	103.6	262.6	202.1	77.6	247.5
Polarization Angle[4] (^{O})	56.6	37.9	55.5	89.2	89.7	23.6	52.8	74.7
Range Resolution (km)	1.08	0.33	0.27	2.50	1.40	3.04	1.00	1.00
Azimuth Resolution (km)	0.53	0.22	0.26	1.00	0.32	3.68	0.89	1.00
Titan True Anomaly (^{O})	16	15	71	69	68	68	246	245

Table B.2: Quantitative constraints of a region of land near to TFL1 from each radar image and the most relevant observational parameters. The area of the region is 143.3 km^2. 1 - Normalized Radar Cross Section; 2 - One standard deviation; 3 - Clockwise from North; 4 - The Cassini Titan RADAR mapper transmits and receives in the same linear polarization and the polarization angle is defined as the angle between the electric field vector and the plane of incidence.

	T25	T29	T64	T91	T92	T95	T104	T108
Date	02/22/07	04/26/07	12/27/09	05/23/13	07/10/13	10/14/13	08/21/14	01/11/15
NRCS[1] (linear)	0.1798	0.2571	0.1576	1.8253	0.9058	0.1899	0.4411	0.5249
NRCS Uncertainty[2] (linear)	0.0057	0.0050	0.0034	0.3634	0.0321	0.0149	0.0209	0.0297
NRCS Noise Floor (linear)	0.0066	0.0015	0.0007	0.0010	0.0017	0.0404	0.0064	0.0014
Incidence Angle (^{O})	20.0	18.4	37.1	3.5	6.1	27.2	10.1	9.4
Azimuth Angle[3] (^{O})	86.8	38.8	246.3	101.6	262.1	201.0	77.6	241.8
Polarization Angle[4] (^{O})	55.0	81.7	44.9	87.9	89.8	23.9	36.0	79.0
Range Resolution (km)	1.07	0.51	0.24	2.50	1.29	2.93	1.56	1.00
Azimuth Resolution (km)	0.55	0.31	0.24	1.00	0.33	3.71	1.17	1.00
Titan True Anomaly (^{O})	16	15	71	69	68	68	246	245

Table B.3: TFL2 quantitative constraints from each radar image and the most relevant observational parameters. The region of TFL2 was defined by a manual mapping of the anomalously bright region in the T104 image while excluding areas that were not observed in all seven flybys. 1 - Normalized Radar Cross Section; A negative NRCS is nonphysical. An estimate of the average noise floor is subtracted from the measured NRCS and statistical fluctuation of the noise floor can result in values slightly less than zero; 2 - One standard deviation; 3 - Clockwise from North; 4 - The Cassini Titan RADAR mapper transmits and receives in the same linear polarization and the polarization angle is defined as the angle between the electric field vector and the plane of incidence; 5 - Indicates TFL2 was not present.

	T25	T29	T64	T91	T92	T104	T108
Date	02/22/07	04/26/07	12/27/09	05/23/13	07/10/13	08/21/14	01/11/15
TFL2 Area (km^2)	✗[5]	✗	✗	✗	✗	321.8	✗
NRCS[1] (linear)	-0.0138	0.0172	0.0008	0.3959	0.0241	0.1257	0.0337
NRCS Uncertainty[2] (linear)	0.0016	0.0004	0.0002	0.0433	0.0005	0.0046	0.0014
NRCS Noise Floor (linear)	0.0040	0.0005	0.0002	0.0015	0.0004	0.0028	0.0003
Incidence Angle (^{O})	19.6	20.4	37.0	3.9	9.5	10.3	7.7
Azimuth Angle[3] (^{O})	66.8	29.1	242.9	270.9	271.3	55.5	217.1
Polarization Angle[4] (^{O})	62.8	82.6	89.2	88.8	75.2	62.4	79.8
Range Resolution (km)	1.05	0.46	0.24	2.50	0.95	1.00	1.00
Azimuth Resolution (km)	0.48	0.30	0.24	1.00	0.33	0.72	1.00
Titan True Anomaly (^{O})	16	15	71	69	68	246	245

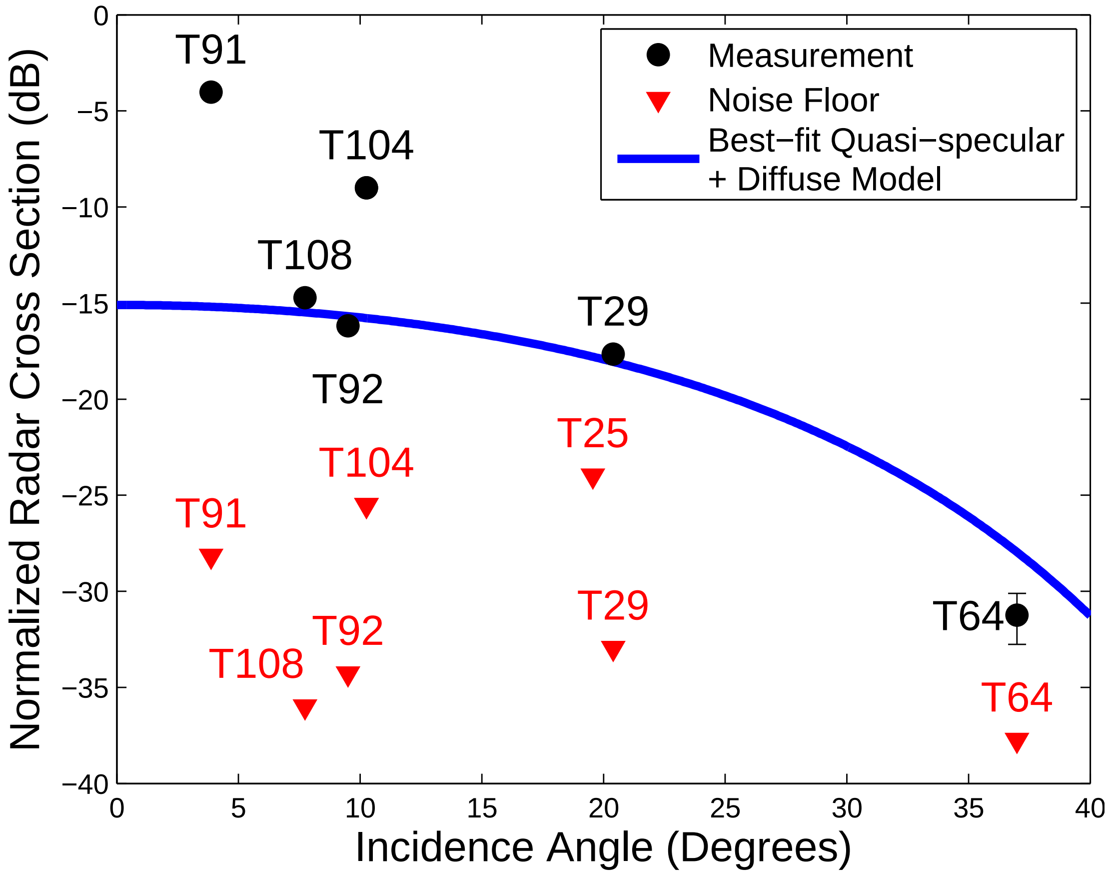

Figure B.2: NRCS of the region of TFL2 as a function of incidence angle. The NRCS does not monotonically increase as the incidence angle decreases and the best-fit quasi-specular plus diffuse model poorly describes the NRCS-incidence angle behavior. Thus the backscatter is inconsistent with a permanent geophysical structure on Titan. The uncertainties of the measurements are included but are smaller than the size of their data points, except for the T64 measurement. The T25 measurement is not shown because it is below its noise floor.

BIBLIOGRAPHY

Aharonson, O., Hayes, A. G., Hayne, P. O., Lopes, R. M., Lucas, A., Perron, J. T., 2014. Titan's surface geology. In: Müller-Wodarg, I., Griffith, C. A., Lellouch, E., Cravens, T. E. (Eds.), Titan. Cambridge University Press.

Aharonson, O., Hayes, A. G., Lunine, J. I., Lorenz, R. D., Allison, M. D., Elachi, C., Dec. 2009. An asymmetric distribution of lakes on Titan as a possible consequence of orbital forcing. Nature Geoscience 2, 851–854.

Atreya, S. K., Adams, E. Y., Niemann, H. B., Demick-Montelara, J. E., Owen, T. C., Fulchignoni, M., Ferri, F., Wilson, E. H., Oct. 2006. Titan's methane cycle. Planet. Space Sci. 54, 1177–1187.

Barnes, J. W., Buratti, B. J., Turtle, E. P., Bow, J., Dalba, P. A., Perry, J., Brown, R. H., Rodriguez, S., Mouélic, S. L., Baines, K. H., Sotin, C., Lorenz, R. D., Malaska, M. J., McCord, T. B., Clark, R. N., Jaumann, R., Hayne, P. O., Nicholson, P. D., Soderblom, J. M., Soderblom, L. A., Jan. 2013. Precipitation-induced surface brightenings seen on Titan by Cassini VIMS and ISS. Planetary Science 2, 1.

Barnes, J. W., Lemke, L., Foch, R., McKay, C. P., Beyer, R. A., Radebaugh, J., Atkinson, D. H., Lorenz, R. D., Le Mouélic, S., Rodriguez, S., Gundlach, J., Giannini, F., Bain, S., Flasar, F. M., Hurford, T., Anderson, C. M., Merrison, J., Ádámkovics, M., Kattenhorn, S. A., Mitchell, J., Burr, D. M., Colaprete, A., Schaller, E., Friedson, A. J., Edgett, K. S., Coradini, A., Adriani, A., Sayanagi, K. M., Malaska, M. J., Morabito, D., Reh, K., Mar. 2012. AVIATR-Aerial Vehicle for In-situ and Airborne Titan Reconnaissance. A Titan airplane mission concept. Experimental Astronomy 33, 55–127.

Barnes, J. W., Soderblom, J. M., Brown, R. H., Soderblom, L. A., Stephan, K., Jaumann, R., Mouélic, S. L., Rodriguez, S., Sotin, C., Buratti, B. J., Baines, K. H., Clark, R. N., Nicholson, P. D., Jan. 2011. Wave constraints for Titan's Jingpo Lacus and Kraken Mare from VIMS specular reflection lightcurves. Icarus 211, 722–731.

Barnes, J. W., Sotin, C., Soderblom, J. M., Brown, R. H., Hayes, A. G., Donelan, M., Rodriguez, S., Le Mouelic, S., Baines, K. H., McCord, T. B., Aug. 2014. Cassini/VIMS Observes Rough Surfaces on Titan's Punga Mare in Specular Reflection. Planetary Science 3, 3.

Bol'shutkin, D. N., Gasan, V. M., Prokhvatilov, A. I., 1971. Temperature dependence of the crystalline lattice parameter of methane in the range of 11-70 K. Journal of Structural Chemistry 12, 670–672.

Brown, R. H., Baines, K. H., Bellucci, G., Bibring, J.-P., Buratti, B. J., Capaccioni, F., Cerroni, P., Clark, R. N., Coradini, A., Cruikshank, D. P., Drossart, P., Formisano, V., Jaumann, R., Langevin, Y., Matson, D. L., McCord, T. B., Mennella, V., Miller, E., Nelson, R. M., Nicholson, P. D., Sicardy, B., Sotin, C., Dec. 2004. The Cassini Visual And Infrared Mapping Spectrometer (Vims) Investigation. Space Sci. Rev. 115, 111–168.

Brown, R. H., Soderblom, L. A., Soderblom, J. M., Clark, R. N., Jaumann, R., Barnes, J. W., Sotin, C., Buratti, B., Baines, K. H., Nicholson, P. D., Jul. 2008. The identification of liquid ethane in Titan's Ontario Lacus. Nature 454, 607–610.

Burr, D. M., Emery, J. P., Lorenz, R. D., Collins, G. C., Carling, P. A., Mar. 2006. Sediment transport by liquid surficial flow: Application to Titan. Icarus 181, 235–242.

Campbell, D. B., Black, G. J., Carter, L. M., Ostro, S. J., Oct. 2003. Radar Evidence for Liquid Surfaces on Titan. Science 302, 431–434.

Chien, J. C. W., 1984. Polyacetylene Chemistry, Physics and Material Science. Academic Press.

Clark, R. N., Curchin, J. M., Barnes, J. W., Jaumann, R., Soderblom, L., Cruikshank, D. P., Brown, R. H., Rodriguez, S., Lunine, J., Stephan, K., Hoefen, T. M., Le Mouélic, S., Sotin, C., Baines, K. H., Buratti, B. J., Nicholson, P. D., Oct. 2010. Detection and mapping of hydrocarbon deposits on Titan. Journal of Geophysical Research (Planets) 115, 10005.

Cordier, D., Mousis, O., Lunine, J. I., Lavvas, P., Vuitton, V., Dec. 2009. An Estimate of the Chemical Composition of Titan's Lakes. The Astrophysical Journal Letters 707, L128–L131.

Coustenis, A., Atreya, S. K., Balint, T., Brown, R. H., Dougherty, M. K., Ferri, F., Fulchignoni, M., Gautier, D., Gowen, R. A., Griffith, C. A., Gurvits, L. I., Jaumann, R., Langevin, Y., Leese, M. R., Lunine, J. I., McKay, C. P., Moussas, X., Müller-Wodarg, I., Neubauer, F., Owen, T. C., Raulin, F., Sittler, E. C., Sohl, F., Sotin, C., Tobie, G., Tokano, T., Turtle, E. P., Wahlund, J.-E., Waite, J. H., Baines, K. H., Blamont, J., Coates, A. J., Dandouras, I., Krimigis, T., Lellouch, E., Lorenz, R. D., Morse, A., Porco, C. C., Hirtzig, M., Saur, J., Spilker, T., Zarnecki, J. C., Choi, E., Achilleos, N., Amils, R., Annan, P., Atkinson, D. H., Bénilan, Y., Bertucci, C., Bézard, B., Bjoraker, G. L., Blanc, M., Boireau, L., Bouman, J., Cabane, M., Capria, M. T., Chassefière, E., Coll, P., Combes, M., Cooper, J. F., Coradini, A., Crary, F., Cravens, T., Daglis, I. A., de Angelis, E., de Bergh, C., de Pater, I., Dunford, C., Durry, G., Dutuit, O., Fairbrother, D., Flasar, F. M., Fortes, A. D., Frampton, R., Fujimoto, M., Galand, M., Grasset, O., Grott, M., Haltigin, T., Herique, A., Hersant, F., Hussmann, H., Ip, W., Johnson, R., Kallio, E., Kempf, S., Knapmeyer, M., Kofman, W., Koop, R., Kostiuk, T., Krupp, N., Küppers, M., Lammer, H., Lara, L.-M., Lavvas, P., Le Mouélic, S., Lebonnois, S., Ledvina, S., Li, J., Livengood, T. A., Lopes, R. M., Lopez-Moreno, J.-J., Luz, D., Mahaffy, P. R., Mall, U., Martinez-Frias, J., Marty, B., McCord, T., Menor Salvan, C., Milillo, A., Mitchell, D. G., Modolo, R., Mousis, O., Nakamura, M., Neish, C. D., Nixon, C. A., Nna Mvondo, D., Orton, G., Paetzold, M., Pitman, J., Pogrebenko, S., Pollard, W., Prieto-Ballesteros, O., Rannou, P., Reh, K., Richter, L., Robb, F. T., Rodrigo, R., Rodriguez, S., Romani, P., Ruiz Bermejo, M., Sarris, E. T., Schenk, P., Schmitt, B., Schmitz, N., Schulze-Makuch, D., Schwingenschuh, K., Selig, A., Sicardy, B., Soderblom, L., Spilker, L. J., Stam, D., Steele, A., Stephan, K., Strobel, D. F., Szego, K., Szopa, C., Thissen, R., Tomasko, M. G., Toublanc, D., Vali, H., Vardavas, I., Vuitton, V., West, R. A., Yelle, R., Young, E. F., Mar. 2009. TandEM: Titan and Enceladus mission. Experimental Astronomy 23, 893–946.

Donelan, M. A., Pierson, W. J., May 1987. Radar scattering and equilibrium ranges in wind-generated waves with application to scatterometry. J. Geophys. Res. 92, 4971–5029.

Elachi, C., Allison, M. D., Borgarelli, L., Encrenaz, P., Im, E., Janssen, M. A., Johnson, W. T. K., Kirk, R. L., Lorenz, R. D., Lunine, J. I., Muhleman, D. O., Ostro, S. J., Picardi, G., Posa, F., Rapley, C. G., Roth, L. E., Seu, R., Soderblom, L. A., Vetrella, S., Wall, S. D., Wood, C. A., Zebker, H. A., Dec. 2004. Radar: The Cassini Titan Radar Mapper. Space Sci. Rev. 115, 71–110.

Elachi, C., van Zyl, J. J., 2006. Introduction to the Physics and Techniques of Remote Sensing: Second Edition. John Wiley and Sons.

Engram, M., Anthony, K. W., Meyer, F. J., Grosse, G., Dec. 2012. Synthetic aperture radar (SAR) backscatter response from methane ebullition bubbles trapped by thermokarst lake ice. Canadian Journal of Remote Sensing 38, 667–682.

Fulchignoni, M., Ferri, F., Angrilli, F., Ball, A. J., Bar-Nun, A., Barucci, M. A., Bettanini, C., Bianchini, G., Borucki, W., Colombatti, G., Coradini, M., Coustenis, A., Debei, S., Falkner, P., Fanti, G., Flamini, E., Gaborit, V., Grard, R., Hamelin, M., Harri, A. M., Hathi, B., Jernej, I., Leese, M. R., Lehto, A., Lion Stoppato, P. F., López-Moreno, J. J., Mäkinen, T., McDonnell, J. A. M., McKay, C. P., Molina-Cuberos, G., Neubauer, F. M., Pirronello, V., Rodrigo, R., Saggin, B., Schwingenschuh, K., Seiff, A., Simões, F., Svedhem, H., Tokano, T., Towner, M. C., Trautner, R., Withers, P., Zarnecki, J. C., Dec. 2005. In situ measurements of the physical characteristics of Titan's environment. Nature 438, 785–791.

Fulchignoni, M., et al., 2006. Huygens HASI Mission Raw and Calibrated Data V1.1, HP-SSA-HASI-2-3-4-MISSION-V1.1, NASA Planetary Data System.

Hayes, A., Aharonson, O., Callahan, P., Elachi, C., Gim, Y., Kirk, R., Lewis, K., Lopes, R., Lorenz, R., Lunine, J., Mitchell, K., Mitri, G., Stofan, E., Wall, S., May 2008. Hydrocarbon lakes on Titan: Distribution and interaction with a porous regolith. Geophys. Res. Lett. 35, 9204.

Hayes, A. G., Aharonson, O., Lunine, J. I., Kirk, R. L., Zebker, H. A., Wye, L. C., Lorenz, R. D., Turtle, E. P., Paillou, P., Mitri, G., Wall, S. D., Stofan, E. R., Mitchell, K. L., Elachi, C., Cassini Radar Team, Jan. 2011. Transient surface liquid in Titan's polar regions from Cassini. Icarus 211, 655–671.

Hayes, A. G., Lorenz, R. D., Donelan, M. A., Manga, M., Lunine, J. I., Schneider, T., Lamb, M. P., Mitchell, J. M., Fischer, W. W., Graves, S. D., Tolman, H. L., Aharonson, O., Encrenaz, P. J., Ventura, B., Casarano, D., Notarnicola, C., Jul. 2013. Wind driven capillary-gravity waves on Titan's lakes: Hard to detect or non-existent? Icarus 225, 403–412.

Hayes, A. G., Wolf, A. S., Aharonson, O., Zebker, H., Lorenz, R., Kirk, R. L., Paillou, P., Lunine, J., Wye, L., Callahan, P., Wall, S., Elachi, C., Sep. 2010. Bathymetry and absorptivity of Titan's Ontario Lacus. Journal of Geophysical Research (Planets) 115, 9009.

Hofgartner, J. D., Hayes, A. G., Lunine, J. I., Zebker, H., Stiles, B. W., Sotin, C., Barnes, J. W., Turtle, E. P., Baines, K. H., Brown, R. H., Buratti, B. J., Clark, R. N., Encrenaz, P., Kirk, R. D., Le Gall, A., Lopes, R. M., Lorenz, R. D., Malaska, M. J., Mitchell, K. L., Nicholson, P. D., Paillou, P., Radebaugh, J., Wall, S. D., Wood, C., Jul. 2014. Transient features in a Titan sea. Nature Geoscience 7, 493–496.

Hofgartner, J. D., Lunine, J. I., Mar. 2013. Does ice float in Titan's lakes and seas? Icarus 223, 628–631.

Jackson, C. R., Apel, J. R., 2004. Synthetic Aperture Radar Marine User's Manual. National Oceanic and Atmospheric Administration.

Jackson, J. D., Jul. 1998. Classical Electrodynamics, 3rd Edition. John Wiley and Sons.

Jennings, D. E., Flasar, F. M., Kunde, V. G., Samuelson, R. E., Pearl, J. C., Nixon, C. A., Carlson, R. C., Mamoutkine, A. A., Brasunas, J. C., Guandique, E., Achterberg, R. K., Bjoraker, G. L., Romani, P. N., Segura, M. E., Albright, S. A., Elliott, M. H., Tingley, J. S., Calcutt, S., Coustenis, A., Courtin, R., Feb. 2009.

Titan's Surface Brightness Temperatures. The Astrophysical Journal Letters 691, L103–L105.

Klimenko, N. A., Gal'Tsov, N. N., Prokhvatilov, A. I., Dec. 2008. Structure, phase transitions, and thermal expansion of ethane C_2H_6. Low Temperature Physics 34, 1038–1043.

Kovacs, A., 1996. Sea Ice Part II. Estimating the full-scale tensile, flexural, and compressive strength of first-year ice. US Army Corps of Engineers, CCREL Report, 96th Edition.

Lide, D. R. (Ed.), 2012. CRC Handbook of Chemistry and Physics, 92nd Edition. CRC Press, Boca Raton, FL, Ch. 6: Fluid Properties, pp. 6–21 – 6–37.

Lora, J. M., Lunine, J. I., Russell, J. L., Hayes, A. G., Nov. 2014. Simulations of Titan's paleoclimate. Icarus 243, 264–273.

Lorenz, R. D., Mitchell, K. L., Kirk, R. L., Hayes, A. G., Aharonson, O., Zebker, H. A., Paillou, P., Radebaugh, J., Lunine, J. I., Janssen, M. A., Wall, S. D., Lopes, R. M., Stiles, B., Ostro, S., Mitri, G., Stofan, E. R., Jan. 2008. Titan's inventory of organic surface materials. Geophys. Res. Lett. 35, 2206.

Lorenz, R. D., Newman, C., Lunine, J. I., Jun. 2010. Threshold of wave generation on Titan's lakes and seas: Effect of viscosity and implications for Cassini observations. Icarus 207, 932–937.

Lorenz, R. D., Oleson, S., Woytach, J., Jones, R., Colozza, A., Schmitz, P., Landis, G., Paul, M., Walsh, J., Mar. 2015. Titan Submarine: Vehicle Design and Operations Concept for the Exploration of the Hydrocarbon Seas of Saturn's Giant Moon. In: Lunar and Planetary Science Conference. Vol. 46 of Lunar and Planetary Science Conference. p. 1259.

Luna, R., Satorre, M. Á., Domingo, M., Millán, C., Santonja, C., Sep. 2012. Density and refractive index of binary CH_4, N_2 and CO_2 ice mixtures. Icarus 221, 186–191.

Lunine, J. I., Atreya, S. K., Mar. 2008. The methane cycle on Titan. Nature Geoscience 1, 159–164.

Lunine, J. I., Hayes, A., Aharonson, O., Mitri, G., Lorenz, R., Stofan, E., Wall, S., Elachi, C., Cassini RADAR Team, Sep. 2009. Evidence for Liquid in Ontario Lacus (Titan) from Cassini-Observed Changes. In: AAS/Division for Planetary Sciences Meeting Abstracts #41. Vol. 41 of AAS/Division for Planetary Sciences Meeting Abstracts. p. #21.04.

Lunine, J. I., Stevenson, D. J., 1985. Evolution of Titan's coupled ocean-atmosphere system and interaction of ocean with bedrock. In: Klinger, J., Benest, D., Dollfus, A., Smoluchowski, R. (Eds.), NATO ASIC Proc. 156: Ices in the Solar System. pp. 741–757.

Lunine, J. I., Stevenson, D. J., Yung, Y. L., Dec. 1983. Ethane ocean on Titan. Science 222, 1229.

Mastrogiuseppe, M., Hayes, A., Poggiali, V., Seu, R., Lunine, J., Hofgartner, J. D., submitted. Radar Sounding Using Cassini Altimeter: Waveform Modeling and Monte Carlo approach for Data Inversion of Observations of Titan Liquid Bodies. IEEE Transactions on Geoscience and Remote Sensing.

Mastrogiuseppe, M., Poggiali, V., Hayes, A., Lorenz, R., Lunine, J., Picardi, G., Seu, R., Flamini, E., Mitri, G., Notarnicola, C., Paillou, P., Zebker, H., Mar. 2014. The bathymetry of a Titan sea. Geophys. Res. Lett. 41, 1432–1437.

Mitchell, K. L., Barmatz, M. B., Jamieson, C. S., Lorenz, R. D., Lunine, J. I., Mar. 2015. Laboratory measurements of cryogenic liquid alkane microwave absorptivity and implications for the composition of Ligeia Mare, Titan. Geophys. Res. Lett. 42, 1340–1345.

Moran, D. W., 1959. Low temperature equilibria in binary systems, including the solid phase. Ph.D. thesis, University of London, Faculty of Engineering.

Muhleman, D. O., Grossman, A. W., Butler, B. J., 1995. Radar Investigations of Mars, Mercury, and Titan. Annual Review of Earth and Planetary Sciences 23, 337–374.

Nakawo, M., 1983. Measurements on air porosity of sea ice. Annals of Glaciology 4, 204–208.

Niemann, H. B., Atreya, S. K., Bauer, S. J., Carignan, G. R., Demick, J. E., Frost, R. L., Gautier, D., Haberman, J. A., Harpold, D. N., Hunten, D. M., Israel, G., Lunine, J. I., Kasprzak, W. T., Owen, T. C., Paulkovich, M., Raulin, F., Raaen, E., Way, S. H., Dec. 2005. The abundances of constituents of Titan's atmosphere from the GCMS instrument on the Huygens probe. Nature 438, 779–784.

Niemann, H. B., Atreya, S. K., Demick, J. E., Gautier, D., Haberman, J. A., Harpold, D. N., Kasprzak, W. T., Lunine, J. I., Owen, T. C., Raulin, F., Dec. 2010. Composition of Titan's lower atmosphere and simple surface volatiles as measured by the Cassini-Huygens probe gas chromatograph mass spectrometer experiment. Journal of Geophysical Research (Planets) 115, 12006.

Omar, M. H., Dokoupil, Z., Schroten, H. G. M., Apr. 1962. Determination of the solid-liquid equilibrium diagram for the nitrogen-methane system. Physica 28, 309–329.

Paillou, P., Lunine, J., Ruffié, G., Encrenaz, P., Wall, S., Lorenz, R., Janssen, M., Sep. 2008. Microwave dielectric constant of Titan-relevant materials. Geophys. Res. Lett. 35, 18202.

Roe, H. G., Grundy, W. M., Jun. 2012. Buoyancy of ice in the CH_4-N_2 system. Icarus 219, 733–736.

Rosenberg, R. M., 1977. Principles of Physical Chemistry. Oxford University Press, New York.

Schinder, P. J., Flasar, F. M., Marouf, E. A., French, R. G., McGhee, C. A., Kliore, A. J., Rappaport, N. J., Barbinis, E., Fleischman, D., Anabtawi, A., 2012. The structure of Titan's atmosphere from Cassini radio occultations: Occultations from the Prime and Equinox missions. Icarus 221 (2), 1020 – 1031.

Schneider, T., Graves, S. D. B., Schaller, E. L., Brown, M. E., Jan. 2012. Polar methane accumulation and rainstorms on Titan from simulations of the methane cycle. Nature 481, 58–61.

Schwander, J., Barnola, J.-M., Andrie, C., Leuenberger, M., Ludin, A., Raynaud, D., Stauffer, B., Feb. 1993. The age of the air in the firn and the ice at Summit, Greenland. Journal of Geophysical Research 98, 2831–2838.

Scott, T. A., Sep. 1976. Solid and liquid nitrogen. Physics Reports 27, 89–157.

Shankaranarayanan, K., Donelan, M. A., Sep. 2001. A probabilistic approach to scatterometer model function verification. J. Geophys. Res. 106, 19969.

Solomonidou, A., Coustenis, A., Hirtzig, M., Rodriguez, S., Stephan, K., Lopes, R. M. C., Drossart, P., Sotin, C., Le Mouélic, S., Lawrence, K., Bratsolis, E., Jaumann, R., Brown, R. H., in press. Temporal variations of Titan's surface with Cassini/VIMS. Icarus.

Sotin, C., Altwegg, K., Brown, R. H., Hand, K., Lunine, J. I., Soderblom, J., Spencer, J., Tortora, P., JET Team, Mar. 2011. JET: Journey to Enceladus and Titan. In: Lunar and Planetary Science Conference. Vol. 42 of Lunar and Planetary Science Conference. p. 1326.

Stephan, K., Jaumann, R., Brown, R. H., Soderblom, J. M., Soderblom, L. A., Barnes, J. W., Sotin, C., Griffith, C. A., Kirk, R. L., Baines, K. H., Buratti, B. J., Clark, R. N., Lytle, D. M., Nelson, R. M., Nicholson, P. D., Apr. 2010. Specular reflection on Titan: Liquids in Kraken Mare. Geophys. Res. Lett. 37, 7104.

Stiles, B. W., Yonggyu, G., Hamilton, G., Hensley, S., Johnson, W. T. K., Shimada, J., West, R. D., Callahan, P., 2006. Ground Processing of Cassini RADAR imagery of Titan. In: Proc. IEEE Conference on RADAR.

Stofan, E., Lorenz, R., Lunine, J., Bierhaus, E. B., Clark, B., Mahaffy, P. R., Ravine, M., 2013. TiME - The Titan Mare Explorer. In: Proceedings of the 2013 IEEE Aerospace Conference. p. 211.

Stofan, E. R., Elachi, C., Lunine, J. I., Lorenz, R. D., Stiles, B., Mitchell, K. L., Ostro, S., Soderblom, L., Wood, C., Zebker, H., Wall, S., Janssen, M., Kirk, R., Lopes, R., Paganelli, F., Radebaugh, J., Wye, L., Anderson, Y., Allison, M., Boehmer, R., Callahan, P., Encrenaz, P., Flamini, E., Francescetti, G., Gim, Y., Hamilton, G., Hensley, S., Johnson, W. T. K., Kelleher, K., Muhleman, D., Paillou, P., Picardi, G., Posa, F., Roth, L., Seu, R., Shaffer, S., Vetrella, S., West, R., Jan. 2007. The lakes of Titan. Nature 445, 61–64.

Tobie, G., Lunine, J. I., Sotin, C., Mar. 2006. Episodic outgassing as the origin of atmospheric methane on Titan. Nature 440, 61–64.

Tokano, T., Mar. 2009. Limnological Structure of Titan's Hydrocarbon Lakes and Its Astrobiological Implication. Astrobiology 9, 147–164.

Tokano, T., Apr. 2013. Are tropical cyclones possible over Titan's polar seas? Icarus 223, 766–774.

Tokano, T., Lorenz, R. D., Jan. 2015. Wind-driven circulation in Titan's seas. Journal of Geophysical Research (Planets) 120, 20–33.

Tokano, T., Lorenz, R. D., in press. Sun-stirred Kraken Mare: Circulation in Titans seas induced by solar heating and methane precipitation. Icarus.

Tokano, T., Lorenz, R. D., Van Hoolst, T., Nov. 2014. Numerical simulation of tides and oceanic angular momentum of Titan's hydrocarbon seas. Icarus 242, 188–201.

Tomasko, M. G., Archinal, B., Becker, T., Bézard, B., Bushroe, M., Combes, M., Cook, D., Coustenis, A., de Bergh, C., Dafoe, L. E., Doose, L., Douté, S., Eibl, A., Engel, S., Gliem, F., Grieger, B., Holso, K., Howington-Kraus, E., Karkoschka, E., Keller, H. U., Kirk, R., Kramm, R., Küppers, M., Lanagan, P., Lellouch, E., Lemmon, M., Lunine, J., McFarlane, E., Moores, J., Prout, G. M., Rizk, B., Rosiek, M., Rueffer, P., Schröder, S. E., Schmitt, B., See, C., Smith, P., Soderblom, L., Thomas, N., West, R., Dec. 2005. Rain, winds and haze during the Huygens probe's descent to Titan's surface. Nature 438, 765–778.

Turtle, E. P., Perry, J. E., Hayes, A. G., Lorenz, R. D., Barnes, J. W., McEwen, A. S., West, R. A., Del Genio, A. D., Barbara, J. M., Lunine, J. I., Schaller, E. L., Ray, T. L., Lopes, R. M. C., Stofan, E. R., Mar. 2011a. Rapid and Extensive

Surface Changes Near Titan's Equator: Evidence of April Showers. Science 331, 1414–1417.

Turtle, E. P., Perry, J. E., Hayes, A. G., McEwen, A. S., Apr. 2011b. Shoreline retreat at Titan's Ontario Lacus and Arrakis Planitia from Cassini Imaging Science Subsystem observations. Icarus 212, 957–959.

Wye, L. C., 2011. Radar scattering from Titan and Saturn's icy satellites using the Cassini spacecraft. Ph.D. thesis, Stanford University, Faculty of Engineering.

Wye, L. C., Zebker, H. A., Lorenz, R. D., Aug. 2009. Smoothness of Titan's Ontario Lacus: Constraints from Cassini RADAR specular reflection data. Geophys. Res. Lett. 36, 16201.

Wye, L. C., Zebker, H. A., Ostro, S. J., West, R. D., Gim, Y., Lorenz, R. D., The Cassini Radar Team, Jun. 2007. Electrical properties of Titan's surface from Cassini RADAR scatterometer measurements. Icarus 188, 367–385.

Zebker, H., Hayes, A., Janssen, M., Le Gall, A., Lorenz, R., Wye, L., Jan. 2014. Surface of Ligeia Mare, Titan, from Cassini altimeter and radiometer analysis. Geophys. Res. Lett. 41, 308–313.

Zebker, H. A., Wye, L. C., Janssen, M. A., Cassini Radar Team, Apr. 2008. Titan's surface from reconciled Cassini microwave reflectivity and emissivity observations. Icarus 194, 704–710.

Zyryanov, V. N., 2012. Physical properties of seawater, including its three phases. Encyclopedia of Life Support, Types and Properties of Water, 1st Edition.